Construction and Building Materials 509 (2026) 145187

Contents lists available at ScienceDirect

Construction and Building Materials

journal homepage: www.elsevier.com/locate/conbuildmat

Investigating the microstructure of mortar systems reinforced with wind turbine blade waste using X-ray computed tomography

Charilaos Paraskevoulakos *, Tao Liu, Ana Teresa Lima

Department of Environmental and Resource Engineering, Technical University of Denmark, Lyngby 2800, Denmark

ARTICLE INFO

Keywords:
X-ray computed tomography (XCT)
Wind turbine blade waste (WTBW)
Porosity
Microstructure
Fibre orientation

ABSTRACT

The potential of valorising shredded end of life wind turbine blades (EoL-WTB) as reinforcement for mortar applications has been only scarcely explored. The relevant studies prove that incorporating WTBW within the mortar matrix can improve the composite strength. However, this reinforcing amplitude varies significantly. Unravelling the corresponding microstructure, which is known to play a pivotal role on the behaviour of fibre-reinforced cement-based composites, remains a knowledge gap until today. This paper attempts to fill this gap via utilising X-ray computed tomography (XCT) to investigate the microstructure of this novel composite. In line with the state-of the-art industry-trail practices, various sizes of the embedded WTBW have been incorporated into the relevant cement matrices. The effect of the waste size on the composite microstructure is determined via probing differences in the porosity behaviour (pore size and spatial distribution and shape factor) and the cement hydration. The spatial distribution and orientation of the WTBW, dispersed within the composite volume, is also investigated. Microstructural observations are linked with the corresponding sample strength. The results reveal the crucial effect of the embedded waste' size on both cement hydration and generated porosity.

1. Introduction

Over the past two decades, the wind energy sector has emerged tremendously, contributing significantly to address the environmental challenges and reduce the carbon emissions, associated with fossil fuel production [1–4]. The anticipated growth of wind farm fleets reveals a complementary issue associated with the waste management [5]. So far, 85–90 % of a wind turbine can be reused or recycled, demonstrating the substantial prospect of this technology being compatible with circular economy; a concept gaining global attention and altering drastically the conventional linear economy approach [6–8]. Metallic parts of a wind turbine, i.e. steel tower and copper cables in addition to the electrical equipment are considered recyclable materials, narrowing the problem of waste management to the blade components [9,10].

Wind turbine blades (WTB) are mainly composed of fiberglass-reinforced polyester or epoxy resins, while carbon fibre is also used as reinforcement. Currently, such materials are considered laborious to be recycled or repurposed with abundant ongoing research exploring chemical and thermal treatment options, all being so far subjected to upscaling challenges [5]. Nowadays, the common practice among the countries investing in the wind energy sector is post-decommissioning landfilling, raising significant concerns about the potential environmental impact. The upcoming global outbreak in wind farms installation is projected to generate million tons of wind turbine blade waste (WTBW), calling for immediate action to be taken [11]. Out of the most promising alternatives with the potential to be implemented in a fast-track mode, is the mechanical disintegration of WTBW. A multiplex process, including sequential shredding, crushing and milling can be adopted to reduce WTBW volume and isolate the key valuable components, being rich in silicon and calcium oxides, to be subsequently utilised as secondary resources in various applications [10–14].

A potential premium beneficiary of a successful implementation of the aforementioned prospect is the construction industry [15]. Construction on a global scale contributes to around 30 % of greenhouse gas emissions, related to human activities [16]. Specifically focusing on carbon dioxide (CO_2), almost 5–8 % of the corresponding worldwide emissions are attributed to the cement production [17]. Concepts of valorising waste that could be utilised as replacement material for cement and aggregates, are currently explored [18–27], with WTBW also being part of this strategy [28–31]. In addition to replacement concepts, the prospect of reinforcing cementitious structures, i.e. concrete, mortar and geopolymer, using WTBW fibrous elements has also

* Correspondence to: DTU Sustain, Brovej, Building 118, 2800 Kgs, Lyngby 2800, Denmark.
E-mail addresses: chapa@dtu.dk (C. Paraskevoulakos), taliu@dtu.dk (T. Liu), atmli@dtu.dk (A.T. Lima).

https://doi.org/10.1016/j.conbuildmat.2026.145187
Received 7 July 2025; Received in revised form 16 December 2025; Accepted 7 January 2026
Available online 12 January 2026

drawn considerable research interest [32–36].

In general, the inclusion of WTBW in the concrete has improved certain composite properties such as decreasing plastic shrinkage, improvement of dimensional stability and flexural strength even after high-temperature, while a slight reduction of compressive strength has been noted, attributed mainly to the poor adhesion of the waste particles to the cementitious matrix as well as the low density of the incorporated waste [26,37]. Despite the growing research footprint within this field, in depth understanding of the physical, chemical and mechanical behaviour of these novel composite materials is lacking.

In this paper, X-ray computed tomography (XCT) has been -for the first time- utilised to address the fundamentals of this novel composite material microstructure. XCT has already proven versatile as an imaging technique to investigate the microstructure of various types of composites [38–40], including cement-based materials [41]. Specific focus has been paid on investigating the pore structure and the distribution of WTBW-fibrous elements within the probed volumes. It is widely accepted that the pore structure is directly associated with the physical and mechanical behaviour of cementitious systems, affecting both their strength, thermal insulation and durability [42–45]. Lower porosity as well as a refined pore size have been linked with higher compressive strength while also improving material resistance to aggressive ions, i.e. chlorides, sulphates penetration. Unlike other fibres, i.e. steel, carbon, polypropylene, utilised to reinforce cementitious structures, uniform geometry and size of post-shredded WTBW material cannot be guaranteed a priori based on current operational planning applications. Thus, the WTBW fibrous elements encapsulated within the cementitious matrix are expected to lie within a wide range of lengths and thicknesses. Such a scatter can drastically affect the performance of the composite structures. It can also affect the mixing process, and subsequently the matrix porosity; a parameter which can dominate the product performance [46–49]. Correlation of this complex microstructure with the mix design and the mechanical properties of WTBW-reinforced cementitious mixes will contribute towards understanding the fundamentals of this novel systems behaviour, ultimately providing the construction industry with composite materials of advanced properties.

2. Materials and equipment

2.1. Materials

WTBW, originally shredded by providers in Spain (Pre Zero), was utilized to prepare the specimen fleet. Further details regarding the material chemical composition and physical properties can be found elsewhere [50]. CEM I 52.5 R (Aalborg White, Denmark) was applied, allowing a rapid hydration reaction, while river sand (0.15 – 4.75 mm) was placed in the mix as a fine aggregate filler. The chemical composition of both WTBW and cement is given in Table 1, as determined via XRF analysis.

As-received WTBW was sieved in-house and separated into four groups based on the passing sieve diameter (0.0063 mm, 0.5 mm, 2 mm, 8 mm). Mortar mix preparation process is described as follows. WTBW, sand and cement powder were all placed in a Hobart mixer and then mixed for 30 s on dry state. Subsequently, water was added and the mixing started, initially at low speed for 60 s, and subsequently at high speed for 2 min. The cementitious slurry mix was placed in a stainless-steel mould cubic grid (25 ×25 x 25 mm) and vibrated for 60 s. The moulds were stored overnight in an environmental chamber at 20 °C with 95 % relative humidity. After being removed from the chamber, specimens were extracted from the moulds, wrapped with plastic sheets and allowed to cure before testing. The sample preparation process is illustrated in Fig. 1. In total, five groups of specimens were produced, four of them containing WTBW of different size and one without waste, acting as the reference state. A uniform 0.5 % WTBW volume fraction was applied in all cases. The mix designs implemented per mortar group and the size of the encapsulated waste are summarised in Table 2.

2.2. Equipment

A Zeiss Xradia 410 Versa microscope was used to perform high-resolution X-ray imaging on representative reference and WTBW-containing mortar specimens. The entire sample volume was probed within the field-of-view (~36 ×36 mm), while the corresponding pixel size was equal to 35.19 μm. Therefore, gel and capillary pores could not be detected, limiting the probed porosity only to macropores and entrapped air voids. X-ray beam was tuned at 140 KV (10 W) with a HE2 filter positioned in place, enabling optimum transmission (20–28 %). Exposure time was set at 1.3 s with 1601 projections being collected, summing the total acquisition duration to 78 min per scan. Bin size was equal to 2. Filtered back projection analytic algorithm was implemented for data reconstruction. The applied scan parameters, summarised in Table 3, were identical for the entire specimen fleet investigated.

Monotonic uniaxial compression (UC) was also performed. Testing was conducted on the entire specimen fleet at a constant loading rate (2400 N/s).

3. Experimental testing and data analysis

3.1. Testing protocol

Five specimens were selected to fulfil the imaging part of the experimental programme, each one representing a single group of those reported in Table 2. Repeated identical scans were acquired at both 28 and 90 days to visualise potential age effect on the cement curing process and the macropore/void structure. Once X-ray imaging at 90 days of sample age was completed, all specimens were subjected to monotonic UC. A 90-day mean compressive strength (triplicate specimens) was determined per group.

3.2. Generic phase segmentation workflow

Post XCT scan acquisition, all the reconstructed datasets were further processed using the data visualisation and analysis commercial software application Avizo [51]. Image registration was performed to align the datasets corresponding to the same specimen, probed at 28 and 90 days. Thus, data analysis on identical material volumes was achieved. Phase segmentation was applied to isolate the embedded parts, including macropore/void volume (low density), hydration products, fine aggregates and WTBW-fibrous elements (medium density) and un-reacted cement grains (high density) [52–54]. A characteristic line scan visualising the different grayscale regions adopted for phase segmentation is given in Fig. 2, along with representative segmented 2D orthoslices.

3.3. WTBW-fibrous elements segmentation workflow

Unlike macropores/voids and unreacted cement, segmentation of

Table 1
Chemical composition of WTBW and cement (wt%) used in the mortar mix design.

Phase	Na_2O	MgO	Al_2O_3	SiO_2	SO_3	K_2O	CaO	TiO_2	Fe_2O_3	Other	LOI*
WTBW	0.86	0.74	5.46	24.85	-	0.25	11.02	0.31	0.18	0.37	55.97
CEM	0.29	0.93	5.27	19.32	3.5	0.33	64.16	-	3.25	0.44	2.45

*LOI = Loss of ignition at 950°C.

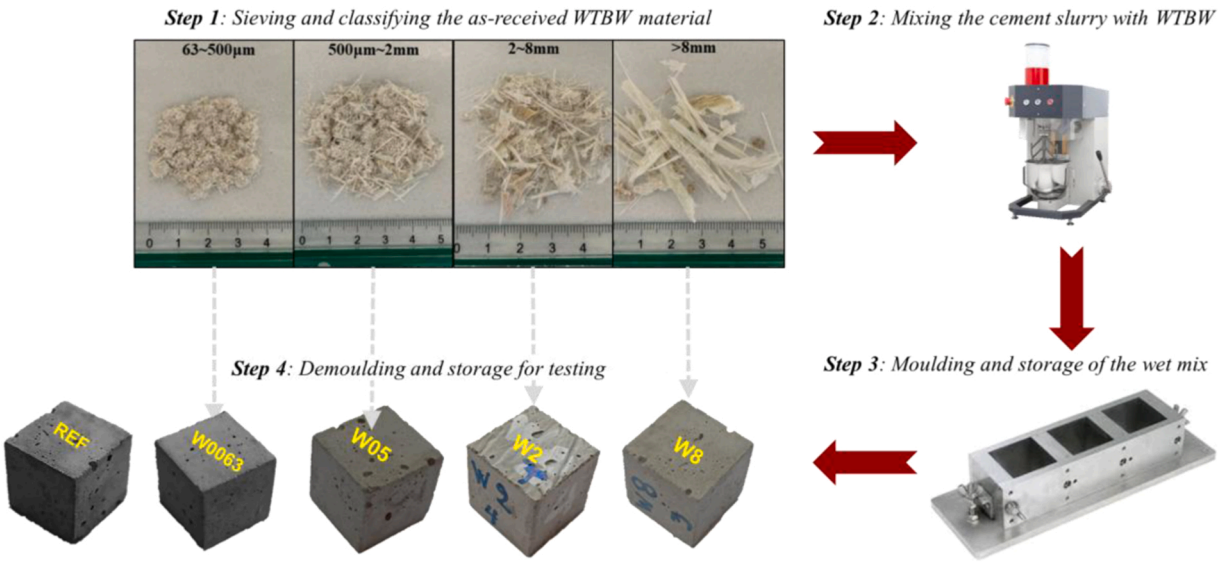

Fig. 1. Schematic overview of the WTBW-mortar preparation process.

Table 2
Mixture proportions of WTBW-mortar group specimens.

Mixture	Reference	W0063	W05	W2	W8
Cement	440 g	440 g	440 g	440 g	440 g
Sand	990 g	990 g	990 g	990 g	990 g
W/C ratio	0.47	0.47	0.47	0.47	0.47
WTBW	-	9.05 g	9.05 g	9.05 g	9.05 g
Size range (mm)	-	0.0063–0.5	0.5–2	2–8	> 8

medium-density particles was more complex. All the corresponding embedded phases, i.e, hydration products, WTBW fibrous elements and fine aggregates, lied within a similar grayscale range. Thus, additional morphological and geometrical operations, were applied to isolate the WTBW parts and enable further data analysis. Manual, visual-based separation of the waste was executed as the last step of the segmentation process to enhance data reliability. The adopted process flow described above is schematically given in Fig. 3.

3.4. Post-phase segmentation workflow

Post phase segmentation, quantitative analysis of the microstructural features followed. Total porosity, macropore/void size and spatial distribution in the 3D domain and 2D porosity area fraction across specimen height were determined. Additional macropore/void features, including morphology/shape factor and sphericity index were highlighted. The un-reacted cement article size and spatial distribution were also quantified. In-depth analysis of the WTBW-fibrous elements was performed, including visualisation of the network, volume fraction and distribution across the specimen height, and preferred orientation. The microstructural features quantified for each specimen probed using XCT are summarised in Fig. 4. Theta (θ) and phi (φ) orientation angles are visualised, following Avizo software sign convention [51,55]. It is worth noting that the term fibrous elements, instead of fibres, has been adopted since the waste encapsulated in the mortar systems consisted of both glass fibre and epoxy resin.

4. Results

4.1. Macropores/voids data analysis

A representative view of the porosity spatial distribution at 28 days, is illustrated in Fig. 5 for all the specimens subjected to X-ray imaging. The corresponding total number of macropores/voids and cumulative macropore/void volume are highlighted in Fig. 6, where a comparison between 28 and 90 days is also illustrated. Accordingly, the change magnitude between 28 and 90 days on each case is quantified and given in Fig. 7. It is worth noting that the total number macropores/voids counted in all five systems seems to decrease with setting time, i.e. from 28 days to 90 days. The trajectory is similar when considering the cumulative macropore volume, albeit the magnitude of change is significantly lower. A deviation is observed in the behaviour of the specimen W0063 when compared to the general trend noted for the rest of the specimens investigated. Instead of a cumulative macropore volume decline, ~13 % rise is observed between 28 days and 90 days of sample curing. A similar observation is noted for specimen W8, which also exhibits a rise in the cumulative macropore/void volume (~8 %), highlighting the complex dynamics of the WTBW-cementitious matrix interaction. Fig. 8 depicts the spatial distribution of macropores/voids across the sample height, as expressed via 2D area fraction porosity, i.e. the percentage of area occupied by macropores/voids at a certain 2D orthoslice across the sample height. The degree of porosity heterogeneity in terms of spatial distribution has been also quantified, enabling comparison between the composite systems. The formula shown below has been employed, where *PH*, *AF* and *Por* stand for the degree of porosity heterogeneity, the 2D porosity (area fraction) and the total porosity.

$$PH = \sum_{i=1}^{N} (AF(i) - Por)^2 \quad (1)$$

A higher PH value indicates a more irregular spatial distribution of the porosity across the sample height. The reference specimen exhibits the most uniform spatial distribution of 2D porosity across its height (PH

Table 3
Scan settings adopted to perform XCT on WTBW-mortar samples.

Microscope	Energy (KV)	Filter	Exposure time (sec)	Projections No.	Bin Size	FOV (mm)	Pixel Size (um)
Versa 410	140	HE2	1.3	1601	2	36 × 36	35.19

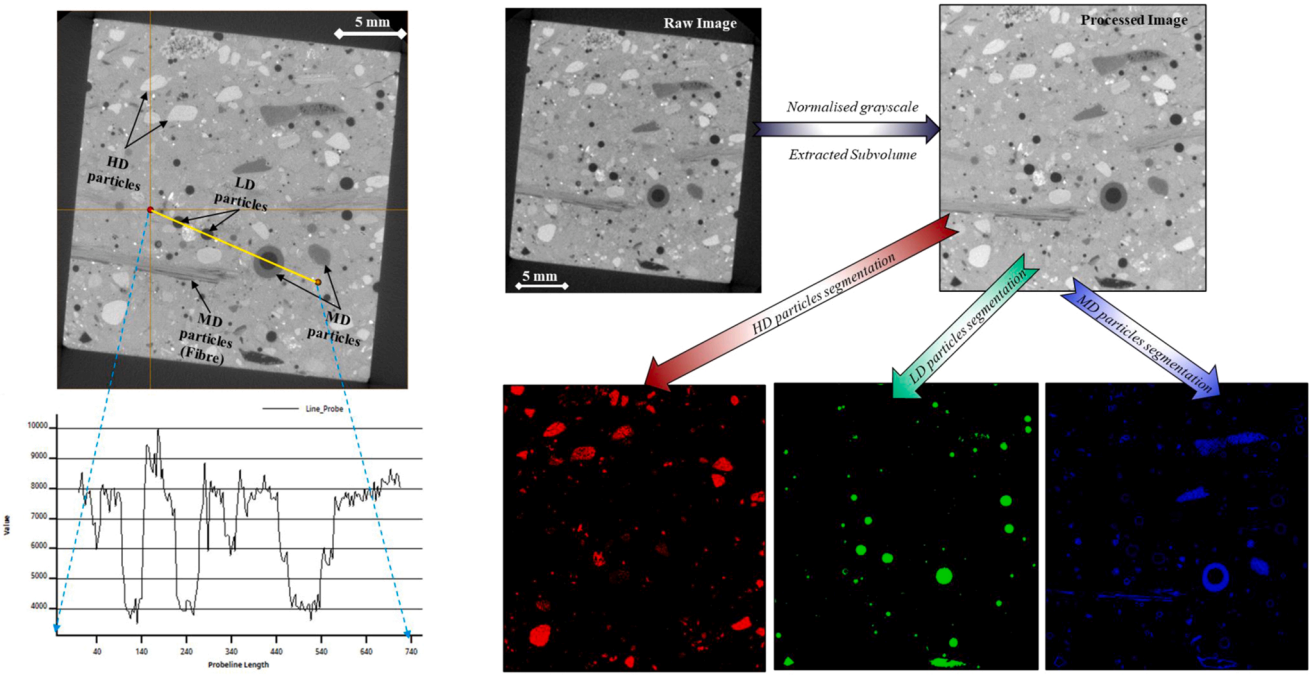

a) Representative 2D orthoslice and segmentation line scan **b)** Post-segmentation representative 2D orthoslice

Fig. 2. Image segmentation protocol illustrating a representative 2D orthoslice with a) an embedded line scan and b) segmented phases. HD (red colour), MD (blue colour) and LD (green colour) stand for high-density, medium-density and low-density particles, respectively.

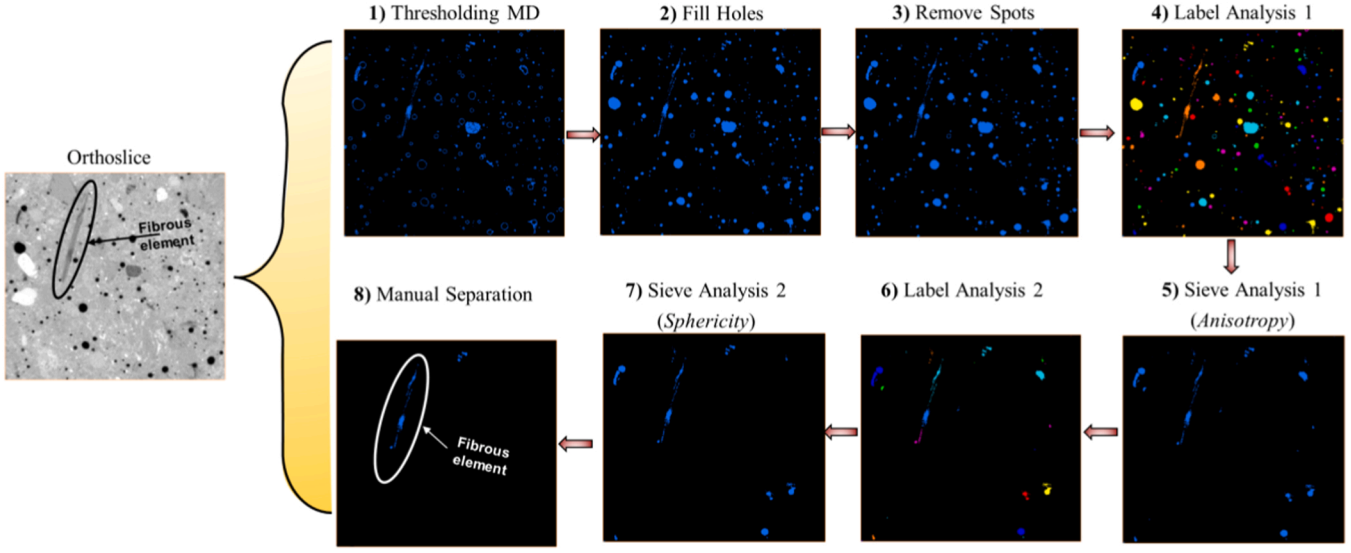

Fig. 3. Schematic illustration of the workflow process followed to segment the WTBW-fibrous elements.

equals 1.21 %). On the contrary specimen W2 indicates the most heterogeneous distribution (PH equals 7.01 %). It is interesting to note that the degree of porosity heterogeneous distribution across the sample height raises with growing size of the embedded WTBW fibrous elements with the only exception being the specimen W8, which indicates a significantly different fibrous element distribution (discussed in the following Section 4.3). Comparison between the specimen 2D porosity distribution across sample height between 28 days and 90 days indicate only minor discrepancies. Pore morphology/shape factor and sphericity index have also been quantified to highlight potential differences among the investigated specimens.

The morphology/shape factor is determined based on the geometric relevance between the three axes within a pore/void. More specifically, the pore is regarded as an ellipsoid, characterised by three perpendicular axes. The three axes length in the perpendicular directions are used to determine the flatness index (*FI*) and the elongation index (*EI*). Considering the lengths of the three axes are characterised by the following relationship: $L_x > L_y > L_z$, then flatness index and elongation index are equal to L_z/L_y and L_y/L_x, respectively. Based on the calculated flatness and elongation index, pores can be divided into four shape types, including i) discoid, ii) spheroid, iii) blade and iv) rod. A Zingg diagram, as shown in Fig. 9, is adopted to separate the macropores based on the various shape types, with the distinction lines, corresponding to both flatness and elongation indices, being placed at 0.67 [43]. The data illustrated correspond to the samples investigated at 28 days. Accordingly, a frequency histogram has been generated and shown in Fig. 10. It

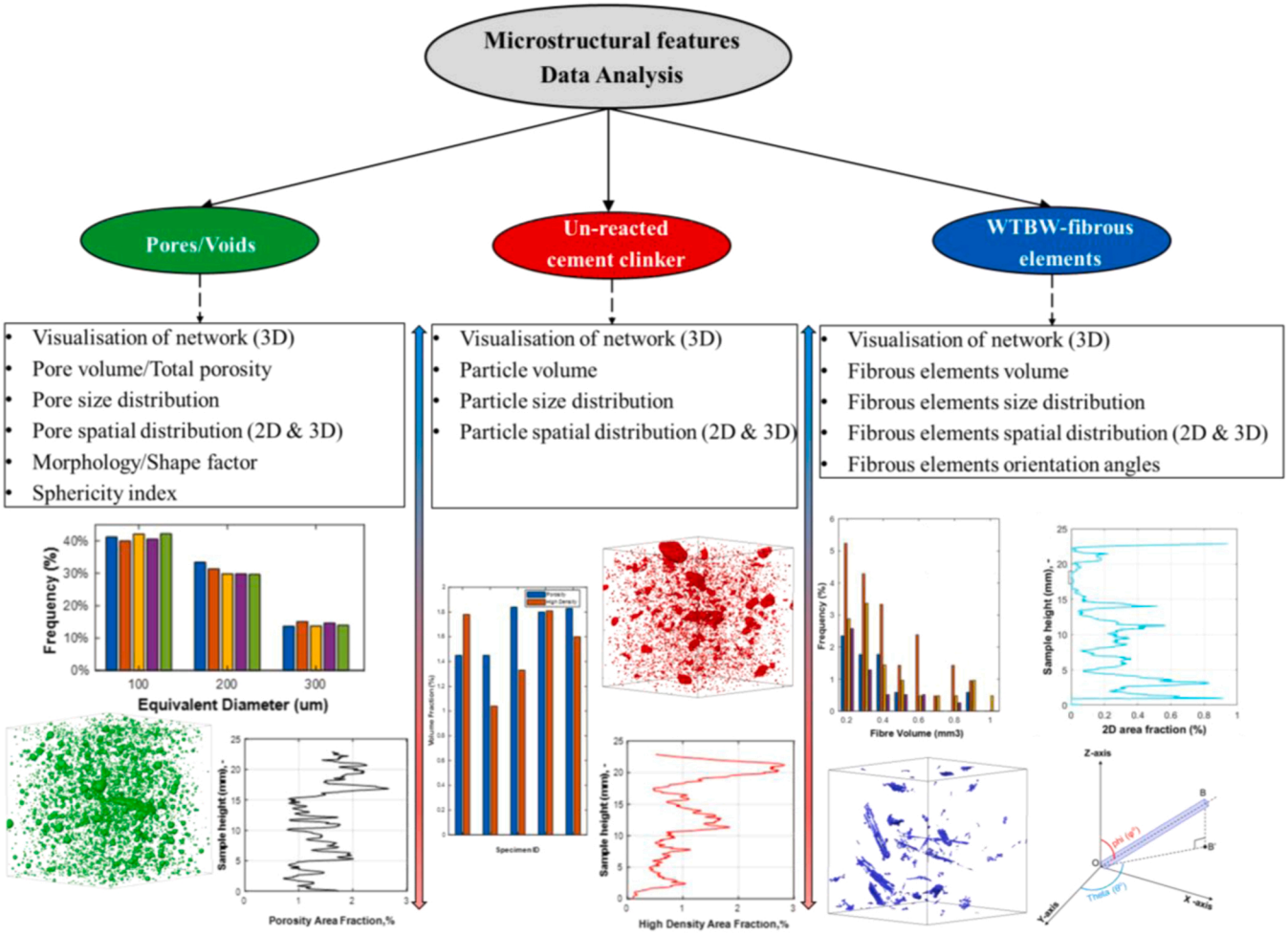

Fig. 4. Schematic illustration of the microstructural feature data analysis and quantification workflow process.

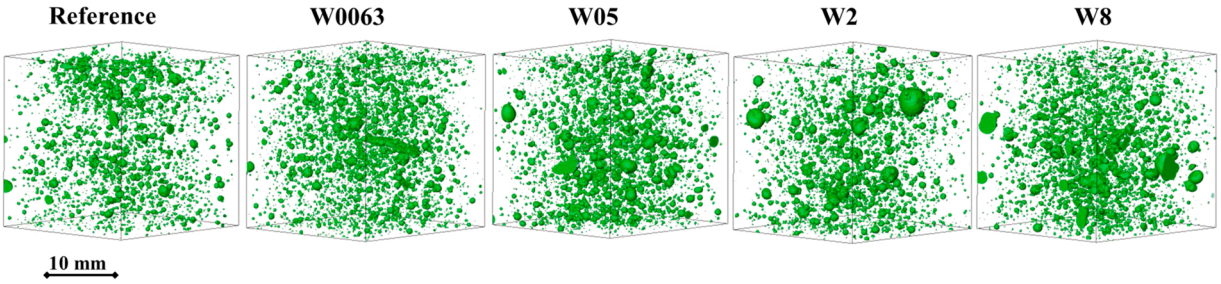

Fig. 5. Representative 3D views of the porosity spatial distribution. Corresponding XCT scans were acquired 28 days after sample preparation.

is noted that spheroid is the dominant shape factor for all the samples fabricated. Among all the macropores segmented and investigated, spherical ones occupy 37 % of the total population in the reference specimen, while the corresponding percentage is higher for all the remaining specimens containing WTBW, with the maximum being specimen W2 (49 %).

Sphericity index is an indicator describing a single pore's shape level of proximity towards an ideal sphere. It ranges between zero and unity, with unity being the case when the pore/void is in shape of a perfect sphere. The sphericity index is calculated based on the following formula:

$$SI = \frac{\pi^{1/3}(6V)^{2/3}}{A} \quad (2)$$

Where *SI* is the sphericity index, *V* is the volume of the macropore/void and *A* is the surface area. The sphericity index distribution at 28 days post sample preparation is given in Fig. 11 for all the specimens investigated. The corresponding variation between 28 and 90 days of sample curing are illustrated for each specimen separately in Fig. 12. It is observed that a significant part of the macropore/void population (~ 86 %) exhibits a sphericity index above 0.9 for the reference specimen. The corresponding percentage is lower in all cases of WTBW-mortar specimens. A noticeable change in pore sphericity index distribution with sample aging is also observed (Fig. 12). In all cases, the percentage of macropores/voids resembling a sphere, i.e. sphericity index above 0.9, grows from 28 to 90 days of sample age. The sharpest rise is shown for specimen W2, where more than 90 % of the macropores/voids resemble a sphere at 90 days, while the corresponding percentage at 28

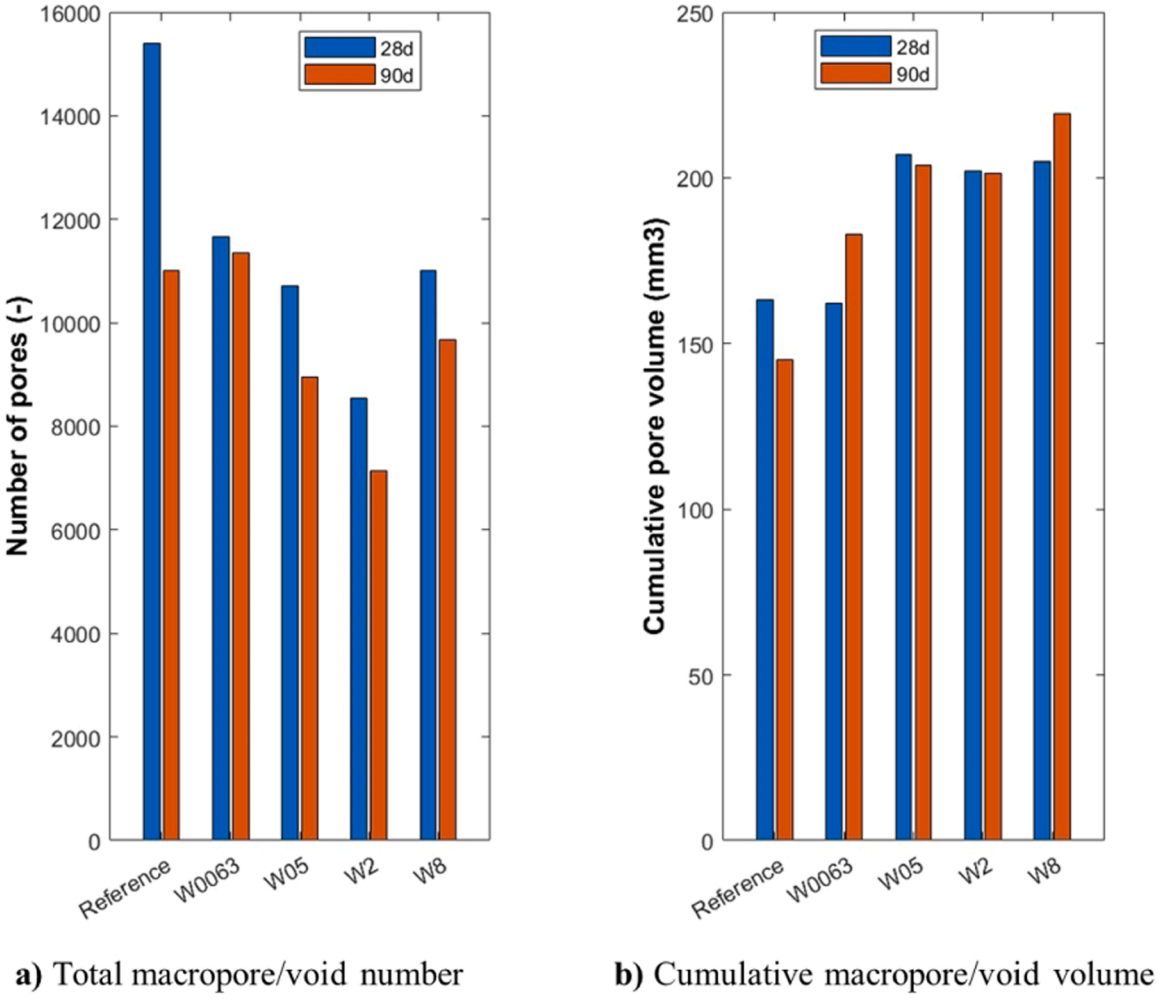

Fig. 6. XCT-derived macropore/void distribution analysis of mortar specimens: a) total macropore/void number and b) cumulative macropore/void volume. Corresponding XCT scans were acquired 28 and 90 days after sample preparation.

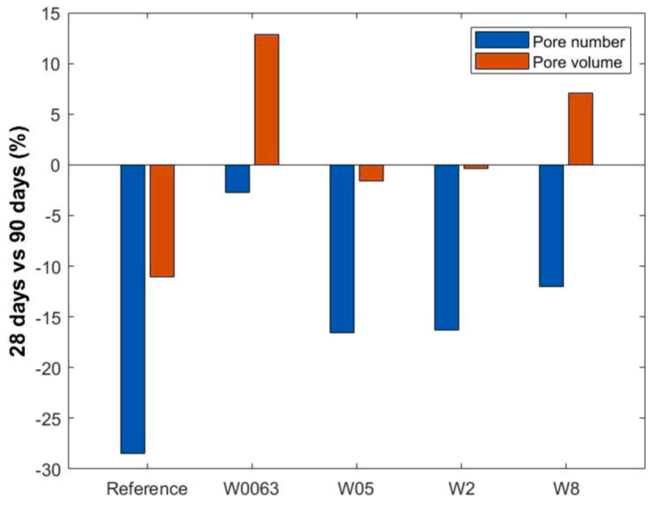

Fig. 7. Shift of cumulative macropore/void number and macropore/void volume observed and quantified between 28 and 90 days of sample age in the specimens investigated using XCT.

days was 43 %.

4.2. Un-reacted cement data analysis

The size and spatial distribution as well as the chronic variation of un-reacted cement phases has been also monitored as cement hydration evolves for all the investigated specimens from 28 to 90 days of sample age. Representative - post phase segmentation - 3D views of these high-density phases at 28 days are shown in Fig. 13. The corresponding cumulative volumes at 28 and 90 days of sample age, are given in Fig. 14a along with the percentage of change for each mix design (Fig. 14b). A considerable decline in the volume of un-reacted cement phase is observed for specimens W0063 (~50 %) and W05 (~20 %), implying that cement hydration is progressing during this period, i.e. from 28 to 90 days. The reference, W2 and W8 specimens exhibit a negligible deviation (less than 10 %) between 28 and 90 days indicating that cement hydration is relatively stable beyond the 28 days. The 2D area fraction distribution of these high-density phases (mainly attributed to un-reacted cement phases) across the sample height is observed in Fig. 15. Only negligible differences can be spotted for the reference, W2 and W8 specimens between 28 and 90 days, while a uniform decline of area fraction across the sample height is observed for specimens W0063 and W05, implying an ongoing, steady-rate hydration of the un-reacted cement phases after the 28 days.

4.3. WTBW-fibrous elements data analysis

The spatial distribution of WTBW-fibrous elements embedded within

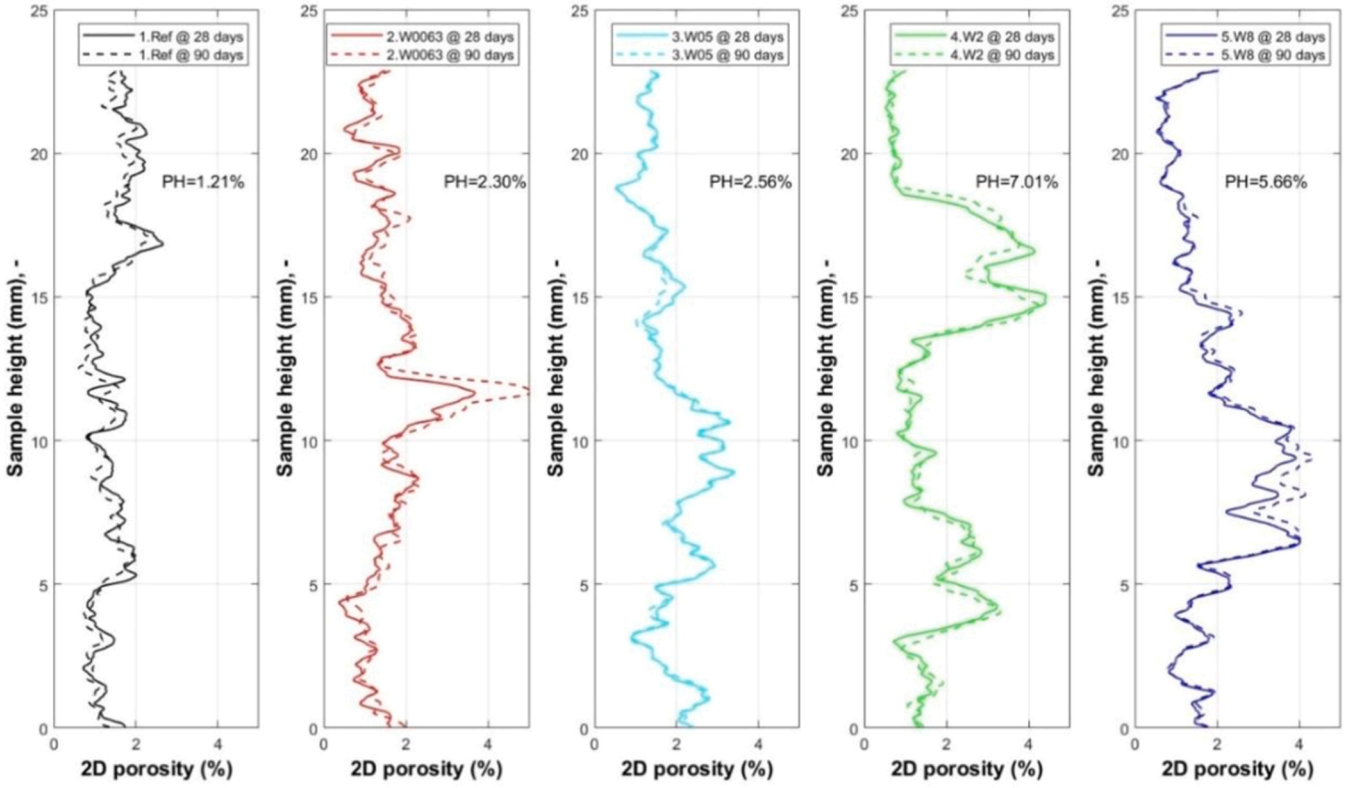

Fig. 8. 2D porosity area fraction distribution across sample height.

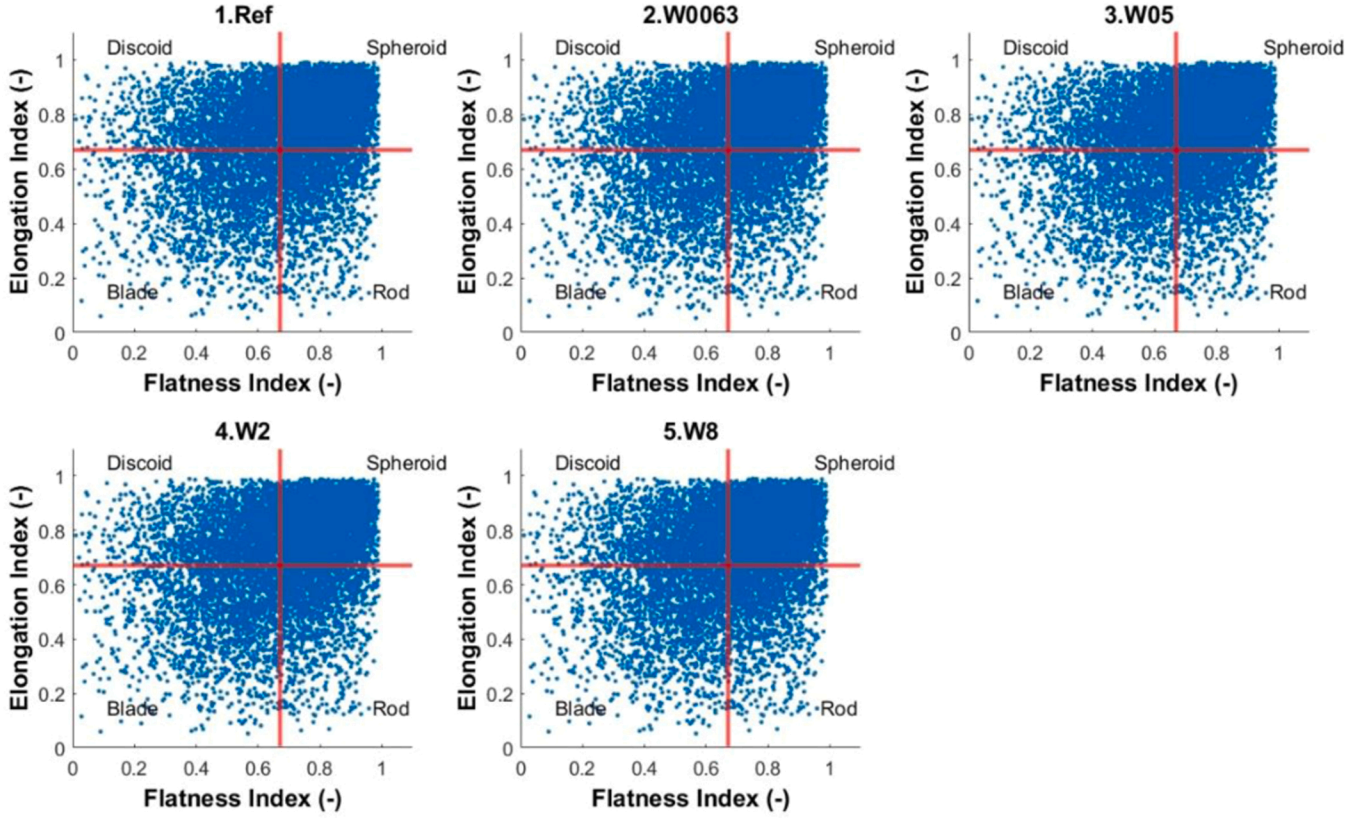

Fig. 9. Zingg diagram illustrating the macropore/void shape classification within the samples investigated at 28 days of sample age.

the waste-containing cementitious specimens is given in Fig. 16. The 3D views illustrated correspond to 28 days of sample age. The fibrous

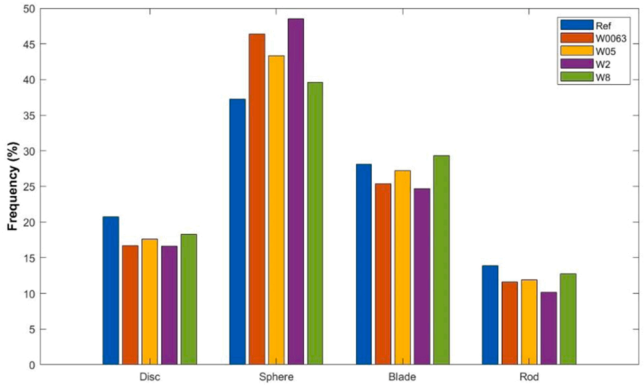

Fig. 10. Pore morphology/shape factor distribution within the samples WTBW-mortar samples investigated at 28 days of sample age.

volume fraction has been calculated for each specimen to estimate potential deviation from the uniformly applied 0.5 % volume fraction operated while preparing the mortar batches and subsequently filling the various mould grid parts. The cumulative volume and the corresponding volume fraction of the fibrous elements within the mortar specimens is illustrated in Fig. 17. Fig. 18 shows the 2D area fraction distribution of WTBW-fibrous elements across the sample height. No comparison between 28 days and 90 days is illustrated, since the fibrous element segmentation is a complex process incorporating manual visual operation and potential deviation of the corresponded yielded volumes could lead to erroneous results. The fibrous volume fraction is less than 0.5 % for all the specimens except for W8 which approaches 0.8 %, exhibiting a relatively non-uniform distribution among the specimens as expected. Even though the majority of fibrous elements reside at the bottom part of the specimens (Fig. 18), parts are also detected throughout the entire mortar volume. Indicatively, a large piece of waste is almost floating at the top of specimen W8. The presence of such a voluminous waste part residing at the top surface of the specimen is expected to affect significantly the specimen performance, potentially underlying the paradoxes spotted and reported in the above regarding porosity volume increase during sample curing (Fig. 7), and reduced porosity heterogeneity *PH* (Fig. 8).

For the case study presented herein, WTBW-fibrous elements used for reinforcement originate from a shredding process that cannot guarantee a uniform shape and length of the valorised material. As a result, a wide range of waste lengths and sizes have been utilised to fabricate the specimens, simulating the currently projected industrial scale scenario. Fibrous element size distribution showed that the larger fibrous waste parts (>0.01 mm^3) occupy more than 99 % of the cumulative volume. Thus, only those parts were further analysed with emphasis given on the preferred orientation, a material property affecting the composite mechanical performance. The distribution of both theta (θ) and phi (φ) orientation angles for all the fibrous elements segmented is visualised in Fig. 19 for the entire specimen fleet. A preferred phi orientation angle (>70°) can be spotted in all cases, implying that fibrous elements tend to settle in parallel to the horizontal plane as the fresh mortar settles (Fig. 4). Theta orientation angle distribution is relatively uniform, not exhibiting any pronounced preferred orientation. Potential link between fibrous element volume and corresponding orientation angle was also studied and the results are illustrated in Fig. 20. The mean orientation angles are relatively consistent even after applying volume filters to isolate the macro-fibrous parts. Specimen W2 exhibits a more diverse range of phi orientation angles for the embedded macrofibres exceeding 1 mm^3, as can be observed in the corresponding spatial distribution and the higher standard deviation.

4.4. Mechanical behaviour of WTBW-mortar composites

Uniaxial compression strength tests have been performed for all the sample groups fabricated, including the reference. Relevant data were collected only at 90 days of sample curing. The results are illustrated in Fig. 21. The incorporation of WTBW-fibrous elements within the cement matrix slightly improves (~2 % - 4 %) the composite compressive strength in all cases, apart from sample W8 where a reduction is noted (-2.2 %). This paradox is attributed to the irregular spatial distribution of WTBW-fibrous elements within the corresponding specimens, as indicatively reported in the previous (Figs. 16,17). Focusing on samples W0063, W05 and W2 a clear trend of compressive strength growth with increasing size of the embedded fibrous material is observed. It is important to clarify that the compressive strength gain noted in Fig. 21 is representative of the entire specimen fleet, considering the uniformly applied 0.5 % fibrous volume fraction. The variations observed in the embedded fibrous volume fraction among the specific specimens subjected to X-ray imaging (Fig. 17), are not expected to affect the above conclusion. Thus, it can be safely regarded that raising the size/thickness of the embedded waste material can increase the composite compressive strength for the same volume fraction.

5. Discussion

The microstructure of WTBW-containing mortar composites has been investigated and reported in the previous. Discrepancies among the fabricated systems were detected and analysed. A holistic comparison among the samples is discussed in this section. Specimen W8 is excluded due to the presence of an excessively large waste piece residing on the sample surface, altering the homogeneity of the corresponding

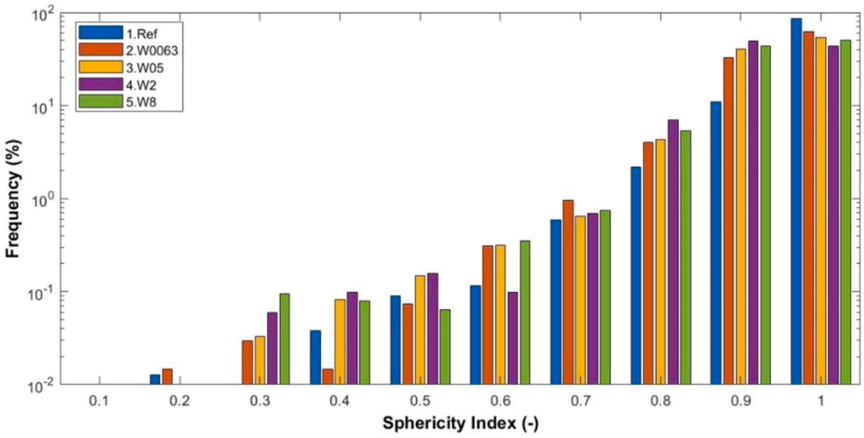

Fig. 11. Pore sphericity index distribution of mortar specimens containing WTBW of various sizes at 28 days of sample age.

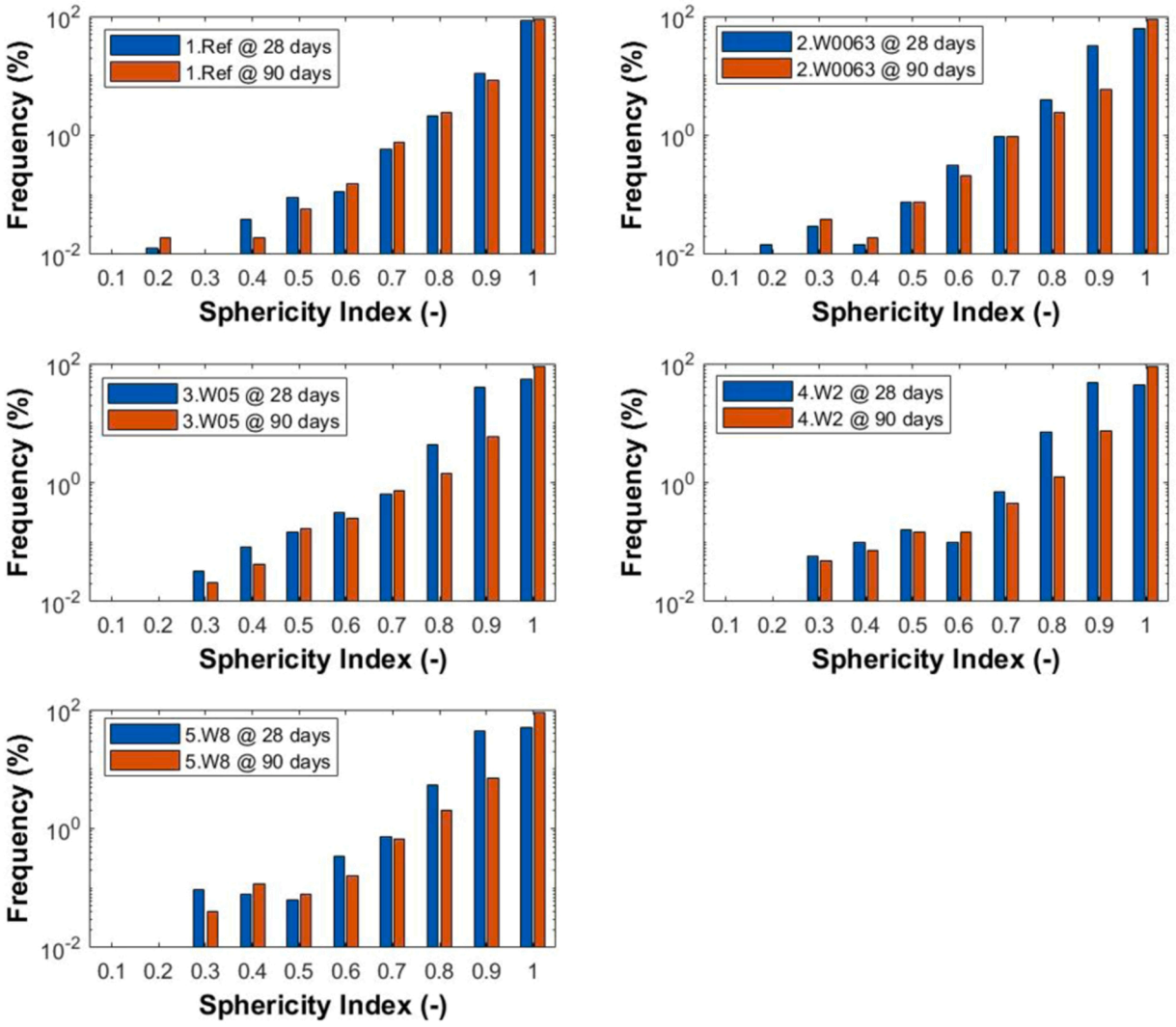

Fig. 12. Sphericity index distribution at 28 and 90 days of sample age for all five mortar systems investigated.

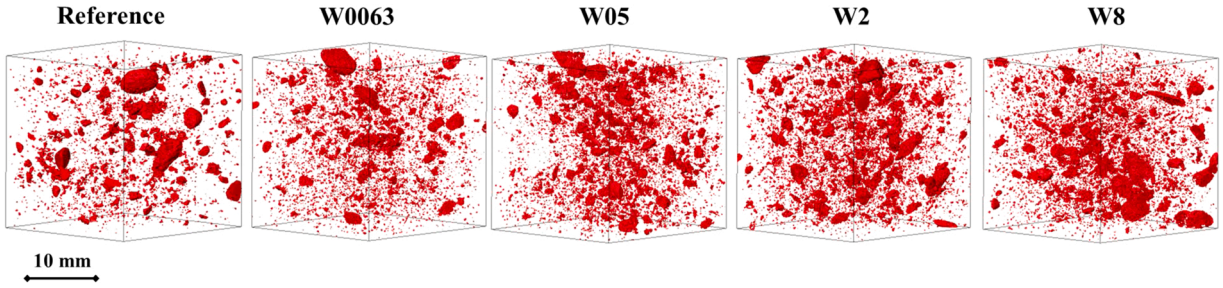

Fig. 13. Representative 3D views of the high-density un-reacted cement phases. Corresponding XCT scans were acquired 28 days after sample preparation.

fabricated specimens. It is worth noting that the segmentation of fibrous elements within the cement matrix, especially the smaller parts, has been significantly complex due to similar densities between the waste and the cement matrix. The implemented data processing workflow analysed in Section 3.3 has efficiently tackled this challenge. However potential marginal differences, especially in regards to the quantitative analysis for the fibrous elements, may persist.

5.1. *Microstructural evolution during aging*

The sample containing small-sized encapsulated waste components (W0063) exhibits a unique behaviour. While all the remaining specimens indicate a relatively negligible reduction in the cumulative macropore/void volume during sample aging (28–90 days), specimen W0063 shows a noticeable growth (Fig. 7). Concurrently, specimen W0063 exhibits a substantial reduction in the volume of un-reacted cement phases during the curing period (Fig. 14), i.e., from 28 day to 90 days. Such behaviour is attributed to the glass–water interaction, which is expected to highly affect both the cement hydration process and the generated pore structure. It is expected that at a primary stage, abundant glassy WTBW particles without an epoxy resin protective layer are dispersed within the cementitious matrix and affect the cement

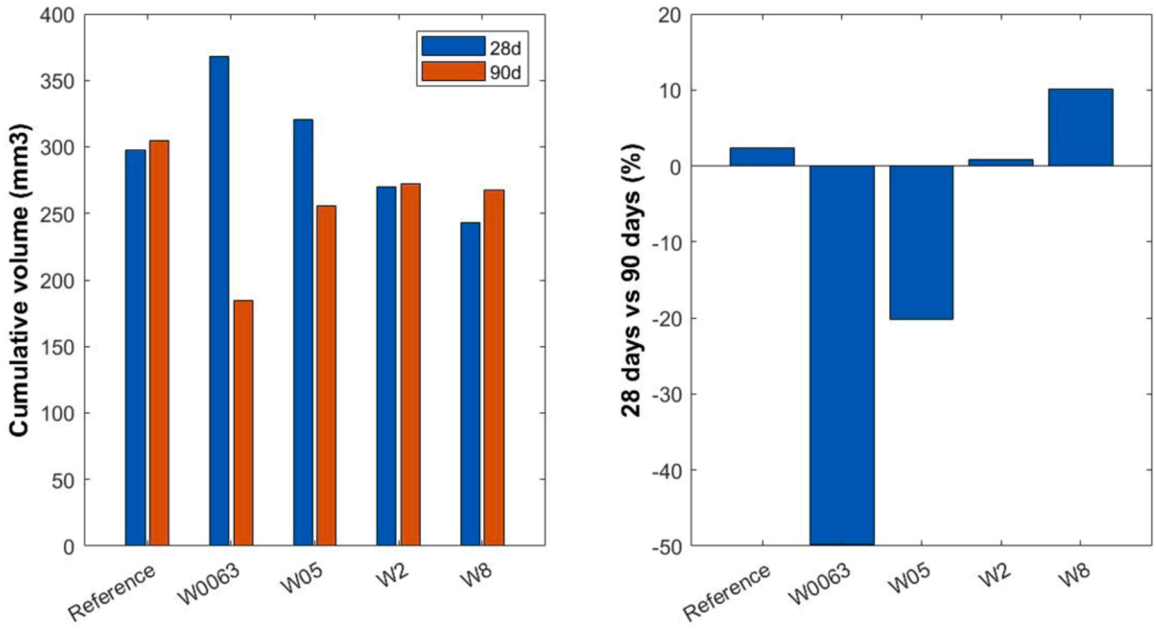

Fig. 14. XCT-derived un-reacted cement phase distribution analysis of mortar specimens: a) cumulative volume, and b) percentage difference between 28 and 90 days of sample age.

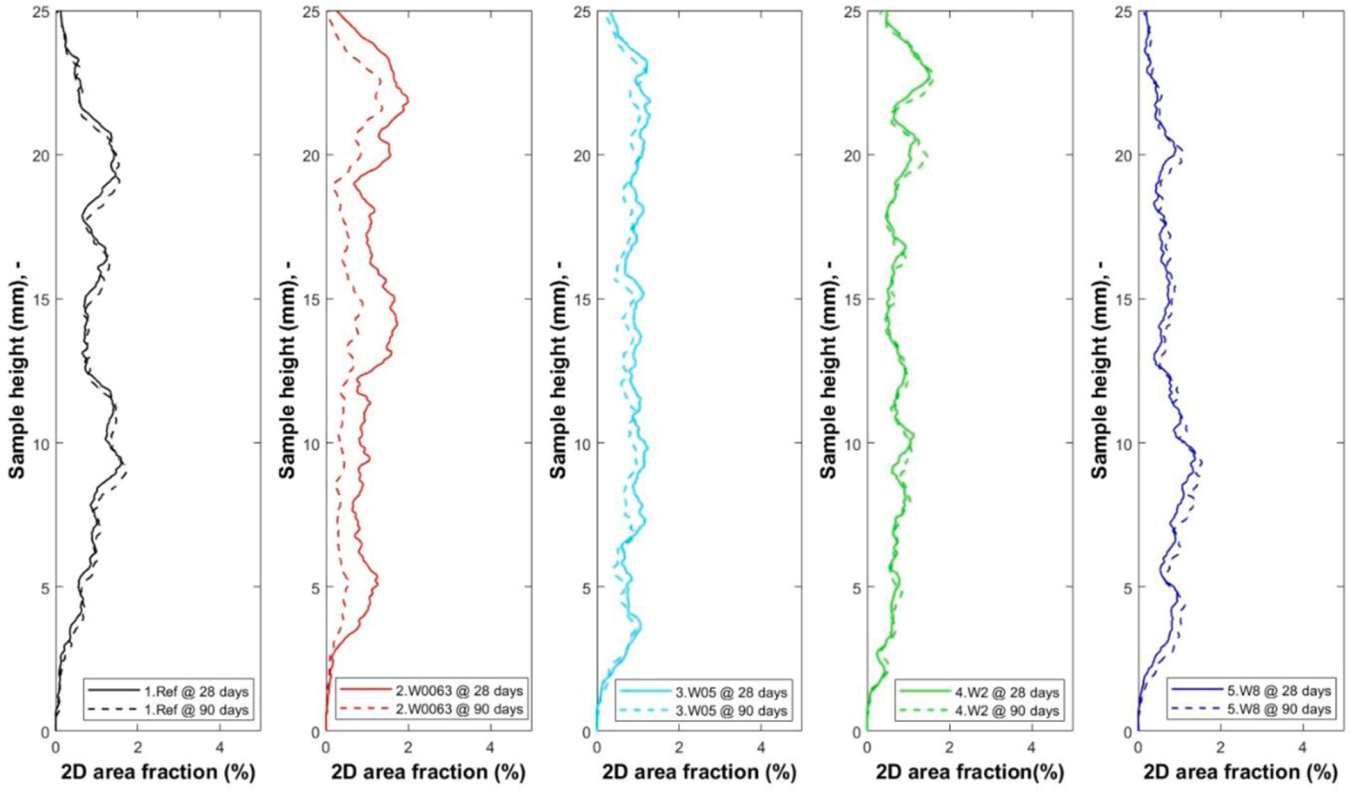

Fig. 15. Distribution of un-reacted cement 2D area fraction across sample height for all the investigated samples.

hydration kinetics via possibly binding part of the alkaline pore solution via glass-alkali reactions. Thus, a delay in cement hydration has occurred, as observed from the high volume of unreacted cement phases at 28 days (W0063). The fact that less pore water is initially available to enable cement hydration due to the abundant glass-water reaction sites is associated with the rise in pore volume observed during the period of 28–90 days (Fig. 7). As the size of the embedded waste grows (W05 & W2), WTBW parts are expected to be confined by epoxy resin, and therefore, less glass-water interfaces are available, minimising the corresponding reaction sites. Thus, cement hydration kinetics is not significantly affected and the pore volume between 28 and 90 days remains relatively constant. The differences spotted with regard to pore network during the curing period are mainly associated with other porosity parameters. The presence of larger fibrous elements affects the

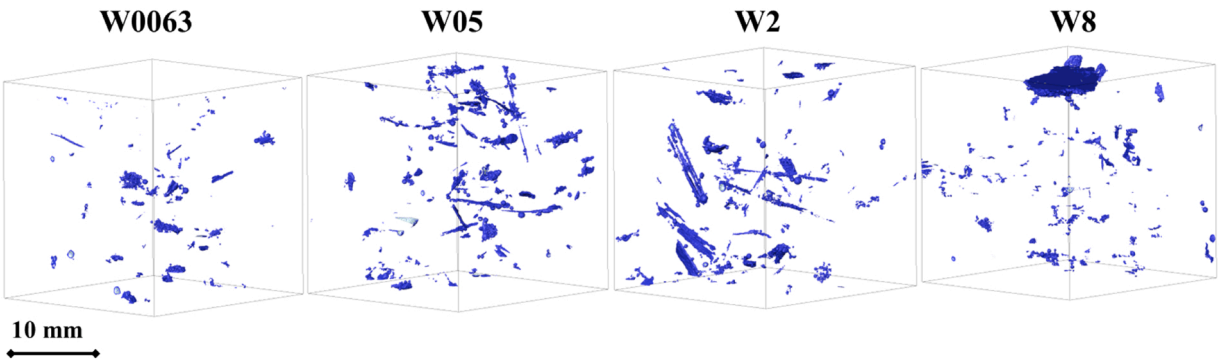

Fig. 16. Representative 3D views of the WTBW-fibrous elements spatial distribution. Corresponding XCT scans were acquired 28 days after sample preparation.

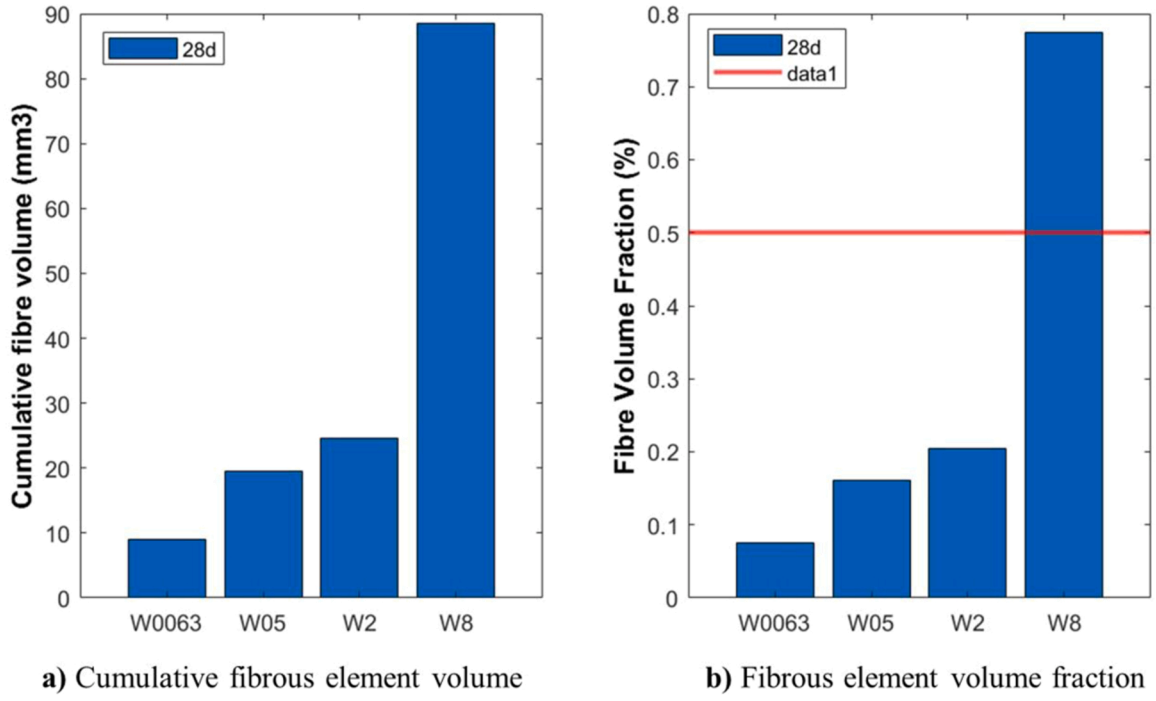

Fig. 17. XCT-derived WTBW-fibrous element phase volume distribution analysis of mortar specimens at 28 days of sample age.

pore sphericity (Fig. 22a) and the percentage of spherical macropores/voids within the entire void population (Fig. 22b). Differences between 28 and 90 days are negligible for the reference case while substantial changes are observed for the WTBW-containing specimens. It is expected that the presence of WTBW fibrous elements affects shrinkage behaviour and, therefore, a delay in the ultimate structure of the porosity network occurs.

Further scientific evidence is required to validate the above hypotheses. Performing chemical characterisation of the phases forming within the composite via X-ray diffraction (XRD) and thermogravimetric analysis (TGA), as well as high magnification microstructural observations via scanning electron microscopy (SEM) and energy dispersive spectroscopy (EDS) could shed light on the behaviour of these novel, complex systems.

5.2. *Microstructure-mechanical strength correlation*

Increasing porosity is well known to be inversely proportional with the compressive strength of cementitious composites. The cumulative volume of the specimen W0063, containing the smallest-sized fibrous elements is lower than in the remaining specimens, containing larger-sized WTBW, while the same applies for the pore heterogeneity (Fig. 8). This finding lies in agreement with the literature, where is has been observed that use of longer fibres, i.e. fibres of larger volume since the fibre diameter is uniform, leads to an increase in the cementitious composite porosity [56–58].

Therefore, considering only the porosity behaviour, specimen W0063 would be expected to exhibit a higher compressive strength that the remaining specimens (W05 and W2), containing larger-sized WTBW. On the contrary, an opposite trend was observed with the compressive strength rising with increasing encapsulated waste size. Screening the macropores characteristics in greater detail highlighted that specimen W2, which exhibited the highest compressive strength, contains the most spherical pores among the remaining specimens (Fig. 10); a factor contributing to an enhanced compressive strength via minimising stress localisation zones. In addition, the pore volume distribution (Fig. 23) clearly indicates that W2 specimen contains the lowest macropores/voids volume if only the small pore (<1 mm^3) range is isolated. Thus, it could be argued that pore morphology/shape factor and volume distribution at the low range, are more critical parameters dictating the compressive strength of WTBW-mortar systems than the total pore/void volume and spatial heterogeneity.

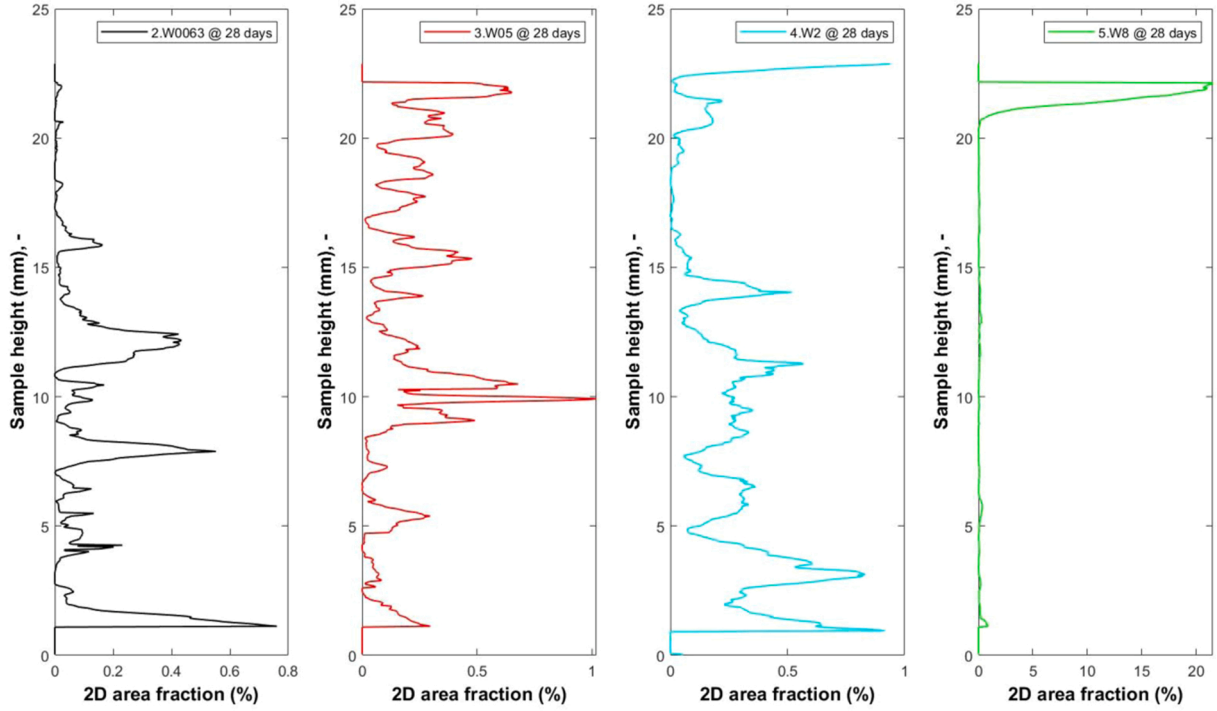

Fig. 18. 2D fibrous element area fraction distribution across sample height.

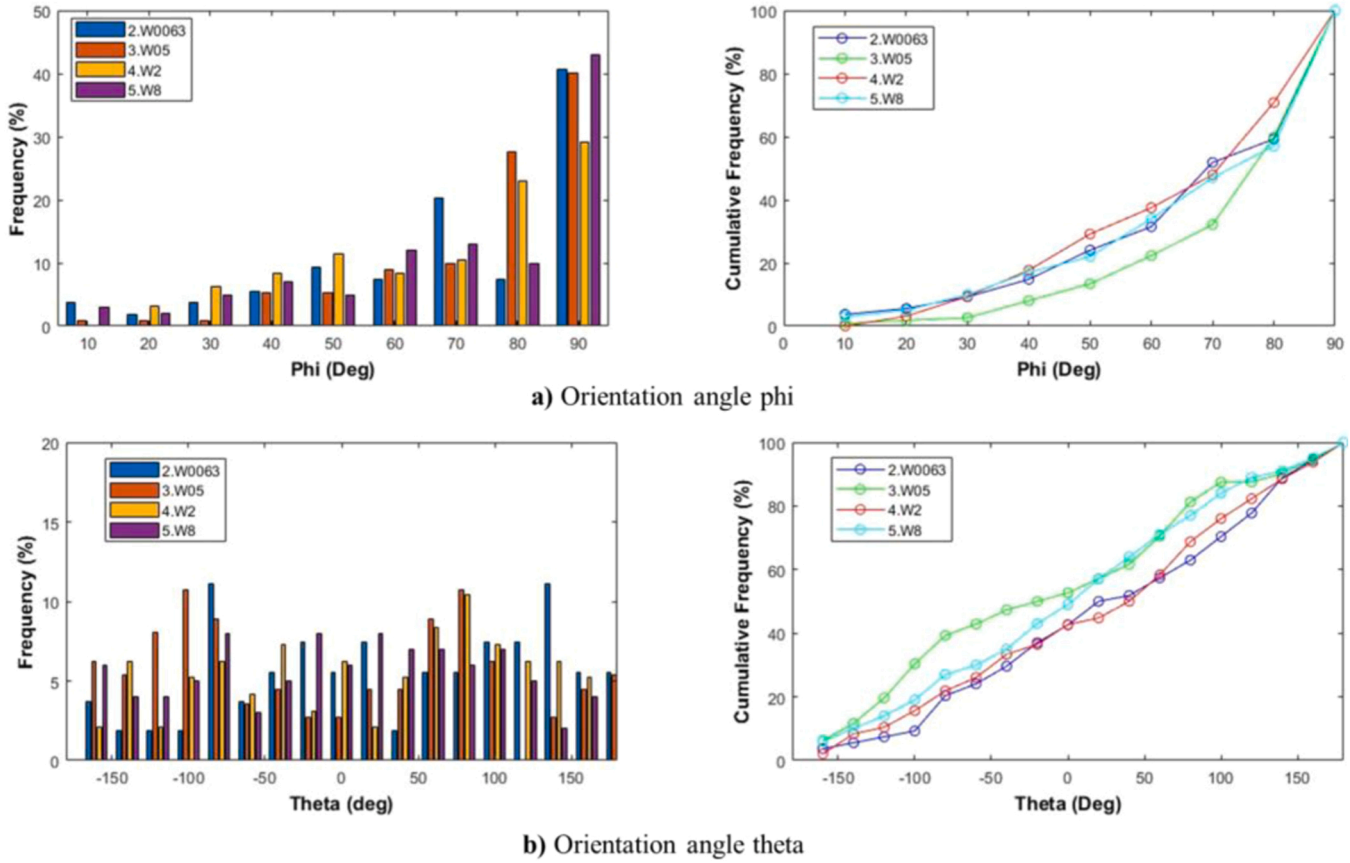

Fig. 19. Distribution of phi and theta orientation angles for the large-sized fibrous elements (>0.01 mm^3) embedded within the entire specimen fleet investigated.

However, the role of fibrous elements contribution to strength gain is also a parameter that needs to be addressed and potentially posing a greater impact on governing the mechanical performance of WTBW-mortar systems than the porosity characteristics. Similar studies performed in concrete specimens, which differ in composition and properties than mortar, have exhibited a narrow rise in compressive strength

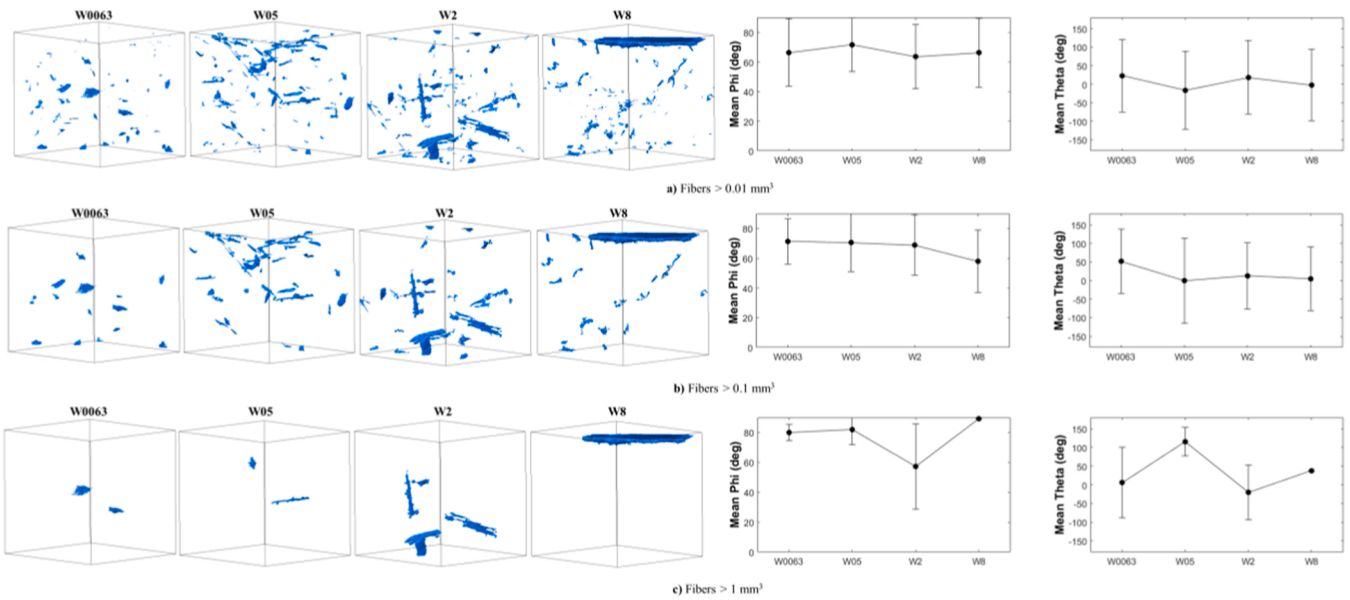

Fig. 20. Distribution of mean phi and theta orientation angles for various volume-discretised ranges of fibrous elements embedded within the specimen fleet investigated.

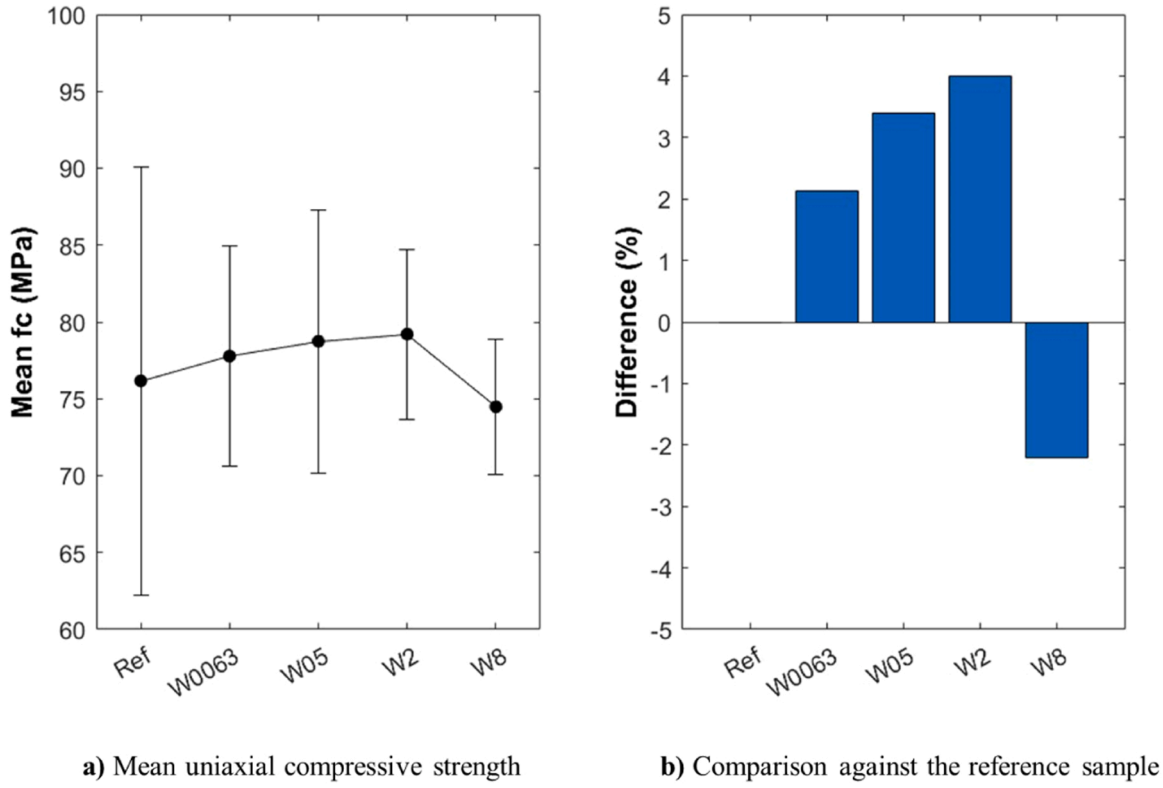

Fig. 21. Uniaxial compressive strength (f_c) variation in a) absolute values and b) comparison against the reference case between the composite samples fabricated and tested.

at similar reinforcement ratios (0.5 % vol.). However, when the addition percentage is increased the compressive strength drops [59,60]. Such a strength gain magnitude is comparable to similar cementitious composite cases where fibres of different materials has been utilised. It is important to note that a direct comparison is not feasible due to the irregular shape and geometry of fibrous elements used in the WTBW case, which differs from surrogate scenarios utilising fibres of uniform size and shape. Even within this context, the results are regarded satisfactory. Experimental trials performed on steel fibre reinforced concrete (SRFC) elements containing a 0.5 % fibre volume fraction exhibit a 3–7 % compressive strength gain [61–63]. The corresponding strength gain when polyvinyl alcohol (PVA) fibres have been used as reinforcement is ~5 % [64], while a 7–15 % reduction has been reported in case of polypropylene fibre (PPF) reinforced concrete composites [65]. Basalt fibres have been also utilized to reinforce concrete elements with the corresponding compressive strength growth lying

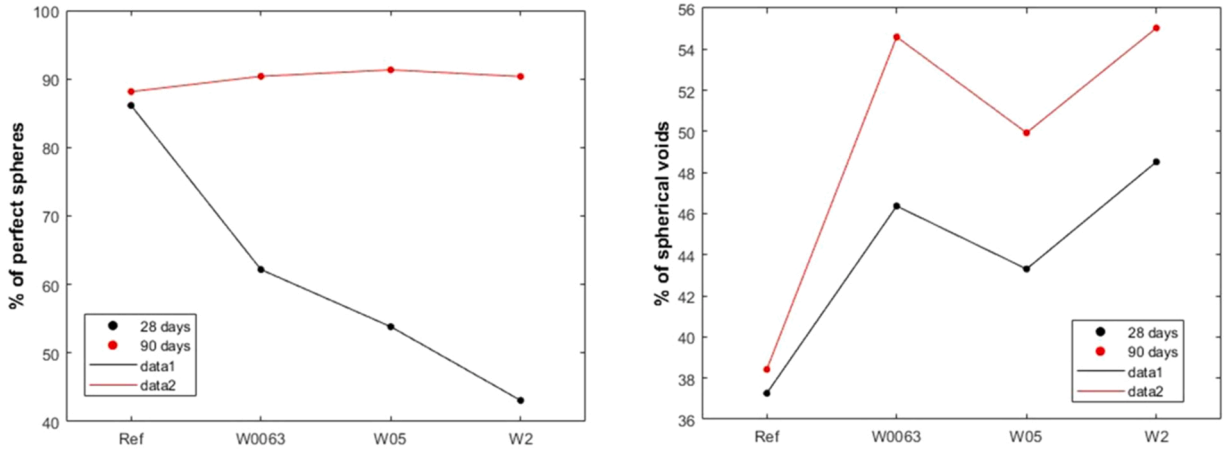

a) Percentage of perfect spheres (Sphericity index > 0.9) **b)** Percentage of spherical voids

Fig. 22. Proportion of voids per sample with a sphericity index exceeding 0.9 at both 28 and 90 days of sample age.

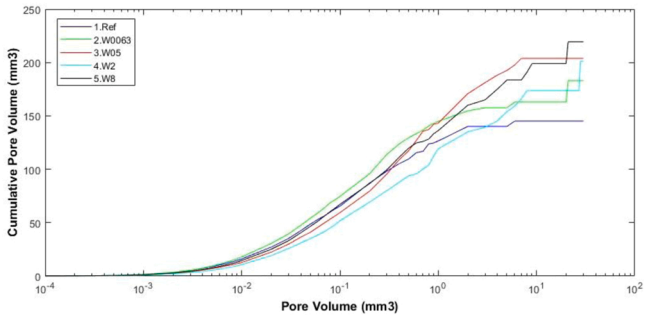

Fig. 23. Pore volume distribution at 90 days of sample age for the entire specimen fleet tested.

between 2 % and 5 % [66–68], while a reduction in strength has been also reported in certain studies [68,69]. Finally, the use of glass fibres has shown fairly promising results leading up to 25 % growth in compressive strength at a 0.5 % volume fraction [65].

Based on the surrogate case studies reported in the previous paragraph, it can be argued that using WTBW parts as reinforcement media for cementitious composites delivers an encouraging and competitive prospect for compressive strength gain, even if the geometry and shape of the embedded fibrous elements cannot be determined and optimised a priori; a significant drawback against the surrogate solutions.

6. Conclusions and recommendations

The potential of WTBW valorisation into the construction industry in the form of mortar strength reinforcement has been discussed in this paper. The experimental programme launched to investigate the above prospect involved the application of XCT in its epicentre, aiming to shed light on previously unchartered territories of the case study. The key findings of the study reported and discussed in the previous are summarized as follows:

- The incorporation of 0.5 % vol. WTBW within the mortar mix can raise compressive strength (2–4 %). The strength gain rises when larger-sized waste elements are embedded within the matrix.
- The use of WTBW within mortar raises both the total volume of macropores/air voids forming and the porosity heterogeneity; two notable factors undermining the mortar strength. However, the macropores/voids forming are more spherical, reducing the available sites for stress localisation zones and, therefore, potentially enhancing the mortar strength.
- The comparison between 28 days and 90 days sample state highlighted the significant role of the waste size in the aging process. Encapsulation of finer waste parts, i.e. W0063, drastically delays the sample curing process – potentially via altering the cement hydration process - and affects porosity formation mechanisms due to ongoing glassy-waster pore reactions. Encapsulation of larger waste parts, i.e. W2, has negligible effect on the sample setting process due to the role of epoxy as a protective barrier between the glassy parts and the cementitious matrix, resembling more the dynamics of a reference system.

Even though the composite strength seems to be only slightly improved via the addition of the fibrous elements, the results compare well against surrogate case studies utilising fibres originating from different materials with the significant advantage of homogenous and optimum geometric properties, i.e. fibre length, shape and thickness. In the scenario of an industrial-scale upgrade for the WTBW post-shredding protocol, facilitating extra steps for sieving and separation of the most promising waste parts, further enhancement of the composite strength mechanical properties, including compressive strength, can be anticipated.

The prospect of valorising EoL-WTBW into cementitious composites has the potential to provide significant support towards a more sustainable future within the construction industry, embracing the principles of circular economy. Future studies are highly recommended to explore the cement hydration kinetics, chemical characterisation and high magnification microstructure properties at the interfaces, using isothermal calorimetry, XRD and SEM, using various sizes of the encapsulated waste. In addition, durability studies on similar mix designs are crucial to gain a more holistic insight into this material behaviour, with special focus given on how the porosity changes - spotted when the WTBW are encapsulated - can affect properties such as shrinkage, water absorption, chloride ingress and carbonation resistance.

CRediT authorship contribution statement

Tao Liu: Writing – review & editing, Resources. **Charilaos Paraskevoulakos:** Writing – original draft, Software, Methodology, Investigation, Formal analysis, Conceptualization. **Ana Teresa Lima:** Writing – review & editing, Project administration, Funding acquisition.

Declaration of Generative AI and AI-assisted technologies in the writing process

The authors declare no use of AI in scientific writing.

Declaration of Competing Interest

The authors declare no Competing Financial or Non-Financial Interests.

Acknowledgements

The presented work is part of the BLADES2BUILD project, funded by the European Union's Horizon Europe Research and Innovation Programme under grant agreement No.101096437. This research is an ongoing effort to promote solutions about recycling, repurposing and reusing of end-of-life wind blade composites. The authors would like to thank the 3D Imaging Centre (3DIM) for providing the relevant software for analysis. Special acknowledgements to PreZero (Spain) for shredding and shipping the WTBW material.

Data availability

Data will be made available on request.

References

[1] Y. Kumar, J. Ringenberg, S.S. Depuru, V.K. Devabhaktuni, J.W. Lee, E. Nikolaidis, et al., Wind energy: Trends and enabling technologies, Renew. Sustain Energy Rev. 53 (2016) 209–224, https://doi.org/10.1016/j.rser.2015.07.200.
[2] S. Roga, S. Bardhan, Y. Kumar, S.K. Dubey, Recent technology and challenges of wind energy generation: A review, Sustain Energy Technol. Assess. 52 (2022) 102239, https://doi.org/10.1016/j.seta.2022.102239.
[3] A. Martinez, L. Murphy, G. Iglesias, Evolution of offshore wind resources in Northern Europe under climate change, Energy 269 (2023) 126655, https://doi.org/10.1016/j.energy.2023.126655.
[4] P. Sadorsky, Wind energy for sustainable development: Driving factors and future outlook, J. Clean. Prod. 289 (2021) 125779, https://doi.org/10.1016/j.jclepro.2020.125779.
[5] R. Fonte, G. Xydis, Wind turbine blade recycling: An evaluation of the European market potential for recycled composite materials, J. Environ. Manag. 287 (2021) 112269, https://doi.org/10.1016/j.jenvman.2021.112269.
[6] J.M.F. Mendoza, A. Gallego-Schmid, A.P.M. Velenturf, P.D. Jensen, D. Ibarra, Circular economy business models and technology management strategies in the wind industry: Sustainability potential, industrial challenges and opportunities, Renew. Sustain Energy Rev. 163 (2022) 112523, https://doi.org/10.1016/j.rser.2022.112523.
[7] A.P.M. Velenturf, A framework and baseline for the integration of a sustainable circular economy in offshore wind, Energies (2021) 14, https://doi.org/10.3390/en14175540.
[8] A. Tyurkay, G.M. Kirkelund, A.T.M. Lima, State-of-the-art circular economy practices for end-of-life wind turbine blades for use in the construction industry, Sustain Prod. Consum 47 (2024) 17–36, https://doi.org/10.1016/j.spc.2024.03.018.
[9] F. Spini, P. Bettini, End-of-Life wind turbine blades: Review on recycling strategies, Compos Part B Eng. 275 (2024) 111290, https://doi.org/10.1016/j.compositesb.2024.111290.
[10] M.Y. Khalid, Z.U. Arif, M. Hossain, R. Umer, Recycling of wind turbine blades through modern recycling technologies: A road to zero waste, Renew. Energy Focus 44 (2023) 373–389, https://doi.org/10.1016/j.ref.2023.02.001.
[11] P. Liu, C.Y. Barlow, Wind turbine blade waste in 2050, Waste Manag 62 (2017) 229–240, https://doi.org/10.1016/j.wasman.2017.02.007.
[12] L. Mishnaevsky, Sustainable end-of-life management of wind turbine blades: Overview of current and coming solutions, Mater. (Basel) 14 (2021) 1–26, https://doi.org/10.3390/ma14051124.
[13] H.K. Jani, S. Singh Kachhwaha, G. Nagababu, A. Das, A brief review on recycling and reuse of wind turbine blade materials, Mater. Today Proc. 62 (2022) 7124–7130, https://doi.org/10.1016/j.matpr.2022.02.049.
[14] E.B. Paulsen, P. Enevoldsen, A multidisciplinary review of recycling methods for end-of-life wind turbine blades, Energies 14 (2021) 1–13, https://doi.org/10.3390/en14144247.
[15] S. Bulińska, A. Sujak, M. Pyzalski, From Waste to Renewables: Challenges and Opportunities in Recycling Glass Fibre Composite Products from Wind Turbine Blades for Sustainable Cement Production, Sustain (2024) 16, https://doi.org/10.3390/su16125150.
[16] N. Labonnote, A. Rønnquist, B. Manum, P. Rüther, Additive construction: State-of-the-art, challenges and opportunities, Autom. Constr. 72 (2016) 347–366, https://doi.org/10.1016/j.autcon.2016.08.026.
[17] R. Kajaste, M. Hurme, Cement industry greenhouse gas emissions - Management options and abatement cost, J. Clean. Prod. 112 (2016) 4041–4052, https://doi.org/10.1016/j.jclepro.2015.07.055.
[18] Z.C. Steyn, A.J. Babafemi, H. Fataar, R. Combrinck, Concrete containing waste recycled glass, plastic and rubber as sand replacement, Constr. Build. Mater. 269 (2021) 121242, https://doi.org/10.1016/j.conbuildmat.2020.121242.
[19] M. Alwaeli, Application of granulated lead-zinc slag in concrete as an opportunity to save natural resources, Radiat. Phys. Chem. 83 (2013) 54–60, https://doi.org/10.1016/j.radphyschem.2012.09.024.
[20] F. Tittarelli, G. Moriconi, Use of GRP industrial by-products in cement based composites, Cem. Concr. Compos 32 (2010) 219–225, https://doi.org/10.1016/J.CEMCONCOMP.2009.11.005.
[21] P. Asokan, M. Osmani, A.D.F. Price, Assessing the recycling potential of glass fibre reinforced plastic waste in concrete and cement composites, J. Clean. Prod. 17 (2009) 821–829, https://doi.org/10.1016/J.JCLEPRO.2008.12.004.
[22] M.C.S. Ribeiro, A.C. Meira-Castro, F.G. Silva, J. Santos, J.P. Meixedo, A. Fiúza, et al., Re-use assessment of thermoset composite wastes as aggregate and filler replacement for concrete-polymer composite materials: A case study regarding GFRP pultrusion wastes, Resour. Conserv Recycl 104 (2015) 417–426, https://doi.org/10.1016/J.RESCONREC.2013.10.001.
[23] J.R. Correia, N.M. Almeida, J.R. Figueira, Recycling of FRP composites: reusing fine GFRP waste in concrete mixtures, J. Clean. Prod. 19 (2011) 1745–1753, https://doi.org/10.1016/J.JCLEPRO.2011.05.018.
[24] H. Wu, J. Gao, C. Liu, Z. Guo, X. Luo, Reusing waste clay brick powder for low-carbon cement concrete and alkali-activated concrete: A critical review, J. Clean. Prod. 449 (2024) 141755, https://doi.org/10.1016/j.jclepro.2024.141755.
[25] X. Li, D. Qin, Y. Hu, W. Ahmad, A. Ahmad, F. Aslam, et al., A systematic review of waste materials in cement-based composites for construction applications, J. Build. Eng. 45 (2022) 103447, https://doi.org/10.1016/j.jobe.2021.103447.
[26] V. Revilla-Cuesta, M. Skaf, J. Manso-Morato, N. Hurtado-Alonso, J.M. Manso, Deepening the effect of selectively crushed wind-turbine blade on the dimensional stability and high-temperature resistance of concrete, J. Build. Eng. 111 (2025) 113440, https://doi.org/10.1016/j.jobe.2025.113440.
[27] D. Trento, F. Faleschini, V. Revilla-Cuesta, V. Ortega-López, Improving the early-age behavior of concrete containing coarse recycled aggregate with raw-crushed wind-turbine blade, J. Build. Eng. 92 (2024) 1–15, https://doi.org/10.1016/j.jobe.2024.109815.
[28] A. Yazdanbakhsh, L.C. Bank, K.A. Rieder, Y. Tian, C. Chen, Concrete with discrete slender elements from mechanically recycled wind turbine blades, Resour. Conserv Recycl 128 (2018) 11–21, https://doi.org/10.1016/J.RESCONREC.2017.08.005.
[29] V. Revilla-Cuesta, M. Skaf, V. Ortega-López, J.M. Manso, Raw-crushed wind-turbine blade: Waste characterization and suitability for use in concrete production, Resour. Conserv Recycl 198 (2023) 107160, https://doi.org/10.1016/j.resconrec.2023.107160.
[30] P.S. Oliveira, M.L.P. Antunes, N.C. da Cruz, E.C. Rangel, A.R.G. de Azevedo, S. F. Durrant, Use of waste collected from wind turbine blade production as an eco-friendly ingredient in mortars for civil construction, J. Clean. Prod. 274 (2020) 122948, https://doi.org/10.1016/J.JCLEPRO.2020.122948.
[31] H. Rodin, S. Nassiri, K. Englund, O. Fakron, H. Li, Recycled glass fiber reinforced polymer composites incorporated in mortar for improved mechanical performance, Constr. Build. Mater. 187 (2018) 738–751, https://doi.org/10.1016/J.CONBUILDMAT.2018.07.169.
[32] D. Baturkin, O.A. Hisseine, R. Masmoudi, A. Tagnit-Hamou, L. Massicotte, Valorization of recycled FRP materials from wind turbine blades in concrete, Resour. Conserv Recycl 174 (2021) 105807, https://doi.org/10.1016/J.RESCONREC.2021.105807.
[33] K. Pławecka, J. Przybyła, K. Korniejenko, W.T. Lin, A. Cheng, M. Łach, Recycling of mechanically ground wind turbine blades as filler in geopolymer composite, Mater. (Basel) (2021) 14, https://doi.org/10.3390/ma14216539.
[34] G.T. Xu, M.J. Liu, Y. Xiang, B. Fu, Valorization of macro fibers recycled from decommissioned turbine blades as discrete reinforcement in concrete, J. Clean. Prod. 379 (2022) 134550, https://doi.org/10.1016/j.jclepro.2022.134550.
[35] B. Fu, K.C. Liu, J.F. Chen, J.G. Teng, Concrete reinforced with macro fibres recycled from waste GFRP, Constr. Build. Mater. 310 (2021) 125063, https://doi.org/10.1016/J.CONBUILDMAT.2021.125063.
[36] L. Senff, R.M. Novais, J. Carvalheiras, J.A. Labrincha, Eco-friendly approach to enhance the mechanical performance of geopolymer foams: Using glass fibre waste coming from wind blade production, Constr. Build. Mater. 239 (2020) 117805, https://doi.org/10.1016/J.CONBUILDMAT.2019.117805.
[37] T. Liu, C. Duyal, C. Paraskevoulakos, K. Enemark-Rasmussen, A. Tyurkay, N. Lushnikova, et al., Effect of wind turbine blade waste on cement hydration and gel structure: Competitive interaction of glass and polyester resin, Compos Part B Eng. (2026) 311, https://doi.org/10.1016/j.compositesb.2025.113273.
[38] J. Holmes, S. Sommacal, R. Das, Z. Stachurski, P. Compston, Digital image and volume correlation for deformation and damage characterisation of fibre-reinforced composites: A review, Compos Struct. 315 (2023) 116994, https://doi.org/10.1016/j.compstruct.2023.116994.
[39] J.P. Forna-Kreutzer, J. Ell, H. Barnard, T.J. Pirzada, R.O. Ritchie, D. Liu, Full-field characterisation of oxide-oxide ceramic-matrix composites using X-ray computed micro-tomography and digital volume correlation under load at high temperatures, Mater. Des. 208 (2021) 109899, https://doi.org/10.1016/J.MATDES.2021.109899.
[40] C. Paraskevoulakos, J. Paul Forna-Kreutzer, K.R. Hallam, C.P. Jones, T.B. Scott, C. Gausse, et al., Investigating the mechanical behaviour of Fukushima MCCI using synchrotron Xray tomography and digital volume correlation, Npj Mater. Degrad. (2022) 6, https://doi.org/10.1038/s41529-022-00264-y.

[41] F. Guo, P.J. Withers, Z. Yang, F. An, Elucidation of cement hydration mechanisms by time-lapse X-ray computed micro-tomography and direct validation of a continuous hydration model, J. Build. Eng. 102 (2025) 111951, https://doi.org/10.1016/j.jobe.2025.111951.
[42] J. Xiao, M. Bai, Y. Wu, Z. Duan, J. Qin, Interlayer bonding strength and pore characteristics of 3D printed engineered cementitious composites (ECC), J. Build. Eng. 84 (2024) 108559, https://doi.org/10.1016/j.jobe.2024.108559.
[43] Y. Guo, X. Chen, B. Chen, R. Wen, P. Wu, Analysis of foamed concrete pore structure of railway roadbed based on X-ray computed tomography, Constr. Build. Mater. 273 (2021) 121773, https://doi.org/10.1016/j.conbuildmat.2020.121773.
[44] Z. Yang, S. Dong, Y. Zhang, Particle packing optimization and pore structure assessment of ternary cementitious system based on X-ray computed tomography and mercury intrusion porosimetry, Constr. Build. Mater. 413 (2024) 134913, https://doi.org/10.1016/j.conbuildmat.2024.134913.
[45] J. Xie, R. Zhang, T. Liu, C. Zhou, T. Gu, B. Chen, et al., Growth of random polyhedral void in structural steel based on micromechanical RVE simulations, Adv. Eng. Softw. 175 (2023) 103344, https://doi.org/10.1016/j.advengsoft.2022.103344.
[46] J. Xiao, Z. Lv, Z. Duan, C. Zhang, Pore structure characteristics, modulation and its effect on concrete properties: A review, Constr. Build. Mater. 397 (2023) 132430, https://doi.org/10.1016/j.conbuildmat.2023.132430.
[47] M.A. Vicente, D.C. González, J. Mínguez, M.A. Tarifa, G. Ruiz, R. Hindi, Influence of the pore morphology of high strength concrete on its fatigue life, Int J. Fatigue 112 (2018) 106–116, https://doi.org/10.1016/J.IJFATIGUE.2018.03.006.
[48] X. Chen, S. Wu, J. Zhou, Influence of porosity on compressive and tensile strength of cement mortar, Constr. Build. Mater. 40 (2013) 869–874, https://doi.org/10.1016/j.conbuildmat.2012.11.072.
[49] G. Ghahremani, A. Bagheri, H. Zanganeh, The effect of size and shape of pores on the prediction model of compressive strength of foamed concrete, Constr. Build. Mater. 371 (2023) 130720, https://doi.org/10.1016/j.conbuildmat.2023.130720.
[50] T. Liu, H. Reascos, U.A. Mughal, G.M. Kirkelund, A.T. Lima, Improving mortar properties with waste wind turbine blade fibers and superplasticizer, Constr. Build. Mater. 472 (2025) 140864, https://doi.org/10.1016/j.conbuildmat.2025.140864.
[51] ThermoFisher Scientific, Avizo 9 user's guide, Thermo Sci. Avizo Softw. 9 Use 'S. Guid (2018) 96–99.
[52] Y.S. Wang, J.G. Dai, X-ray computed tomography for pore-related characterization and simulation of cement mortar matrix, NDT E Int 86 (2017) 28–35, https://doi.org/10.1016/J.NDTEINT.2016.11.005.
[53] C. Zou, G. Long, X. Zeng, K. Ma, Y. Xie, Hydration and multiscale pore structure characterization of steam-cured cement paste investigated by X-ray CT, Constr. Build. Mater. 282 (2021) 122629, https://doi.org/10.1016/j.conbuildmat.2021.122629.
[54] S. Shirani, A. Cuesta, A.G. De la Torre, I. Santacruz, A. Morales-Cantero, I. Koufany, et al., Mix and measure - Combining in situ X-ray powder diffraction and microtomography for accurate hydrating cement studies, Cem. Concr. Res 175 (2024) 1–13, https://doi.org/10.1016/j.cemconres.2023.107370.
[55] B. Yu, J. Ren, K. Wang, C. Wang, H. Bian, Experimental Study on the Characterization of Orientation of Polyester Short Fibers in Rubber Composites by an X-ray Three-Dimensional Microscope, Mater. (Basel) (2022) 15, https://doi.org/10.3390/ma15103726.
[56] L. Wang, T. He, Y. Zhou, S. Tang, J. Tan, Z. Liu, et al., The influence of fiber type and length on the cracking resistance, durability and pore structure of face slab concrete, Constr. Build. Mater. 282 (2021) 122706, https://doi.org/10.1016/j.conbuildmat.2021.122706.
[57] M. Habibi, É. Ruiz, G. Lebrun, L. Laperrière, Effect of surface density and fiber length on the porosity and permeability of nonwoven flax reinforcement, Text. Res J. 88 (2018) 1776–1787, https://doi.org/10.1177/0040517517708542.
[58] G. Xue, E. Yilmaz, W. Song, S. Cao, Fiber length effect on strength properties of polypropylene fiber reinforced cemented tailings backfill specimens with different sizes, Constr. Build. Mater. 241 (2020) 118113, https://doi.org/10.1016/j.conbuildmat.2020.118113.
[59] V. Ortega-López, F. Faleschini, N. Hurtado-Alonso, J. Manso-Morato, V. Revilla-Cuesta, Analysis of raw-crushed wind-turbine blade as an overall concrete addition: Stress–strain and deflection performance effects, Compos Struct. (2024) 340, https://doi.org/10.1016/j.compstruct.2024.118170.
[60] V. Revilla-Cuesta, A.B. Espinosa, R. Serrano-López, M. Skaf, J.M. Manso, Mechanical Properties of Concrete Mixes with Selectively Crushed Wind Turbine Blade: Comparison with Raw-Crushing, Mater. (Basel) (2024) 17, https://doi.org/10.3390/ma17246299.
[61] P.S. Song, S. Hwang, Mechanical properties of high-strength steel fiber-reinforced concrete, Constr. Build. Mater. 18 (2004) 669–673, https://doi.org/10.1016/j.conbuildmat.2004.04.027.
[62] F. Köksal, F. Altun, I. Yiğit, Y. Şahin, Combined effect of silica fume and steel fiber on the mechanical properties of high strength concretes, Constr. Build. Mater. 22 (2008) 1874–1880, https://doi.org/10.1016/j.conbuildmat.2007.04.017.
[63] Ş. Yazici, G. Inan, V. Tabak, Effect of aspect ratio and volume fraction of steel fiber on the mechanical properties of SFRC, Constr. Build. Mater. 21 (2007) 1250–1253, https://doi.org/10.1016/j.conbuildmat.2006.05.025.
[64] K.M.A. Hossain, M. Lachemi, M. Sammour, M. Sonebi, Strength and fracture energy characteristics of self-consolidating concrete incorporating polyvinyl alcohol, steel and hybrid fibres, Constr. Build. Mater. 45 (2013) 20–29, https://doi.org/10.1016/j.conbuildmat.2013.03.054.
[65] Z. Yuan, Y. Jia, Mechanical properties and microstructure of glass fiber and polypropylene fiber reinforced concrete: An experimental study, Constr. Build. Mater. 266 (2021) 121048, https://doi.org/10.1016/j.conbuildmat.2020.121048.
[66] A.B. Kizilkanat, N. Kabay, V. Akyüncü, S. Chowdhury, A.H. Akça, Mechanical properties and fracture behavior of basalt and glass fiber reinforced concrete: An experimental study, Constr. Build. Mater. 100 (2015) 218–224, https://doi.org/10.1016/j.conbuildmat.2015.10.006.
[67] C. Jiang, K. Fan, F. Wu, D. Chen, Experimental study on the mechanical properties and microstructure of chopped basalt fibre reinforced concrete, Mater. Des. 58 (2014) 187–193, https://doi.org/10.1016/j.matdes.2014.01.056.
[68] J. Branston, S. Das, S.Y. Kenno, C. Taylor, Mechanical behaviour of basalt fibre reinforced concrete, Constr. Build. Mater. 124 (2016) 878–886, https://doi.org/10.1016/j.conbuildmat.2016.08.009.
[69] D.P. Dias, C. Thaumaturgo, Fracture toughness of geopolymeric concretes reinforced with basalt fibers, Cem. Concr. Compos 27 (2005) 49–54, https://doi.org/10.1016/j.cemconcomp.2004.02.044.